JACS
JOURNAL OF THE AMERICAN CHEMICAL SOCIETY

pubs.acs.org/JACS
Article

Lipid-siRNA Organization Modulates the Intracellular Dynamics of Lipid Nanoparticles

Yulin Mo, Alexander F. A. Keszei, Shagun Kothari, Heyi Liu, Anni Pan, Paige Kim, Jiachuan Bu, Albert Kamanzi, David L. Dai, Mohammad T. Mazhab-Jafari, Juan Chen,* Sabrina Leslie, and Gang Zheng*

Cite This: J. Am. Chem. Soc. 2025, 147, 10430−10445

ABSTRACT: Lipid nanoparticles (LNPs) are widely used for delivering therapeutic nucleic acids, yet the relationship between their internal structure and intracellular behavior, particularly before RNA release, remains unclear. Here, we elucidate how lipid-siRNA organization within LNPs can modulate their intracellular delivery dynamics. We use cryo-electron microscopy and photochemical assays to reveal that increased siRNA loading can reduce helper lipids' distribution to the LNP surface, while siRNA consistently localizes near the surface. These alterations in lipid-siRNA organization affect LNP membrane fluidity, enhancing LNP fusion with cellular membranes and promoting cytosolic siRNA delivery, primarily via macropinocytosis. Using photosensitive lipids and live cell imaging, we demonstrate that lipid-siRNA organization regulates LNP responsiveness to external stimuli, significantly affecting siRNA endosomal escape efficiency upon light activation. We further confirm this observation using convex lens-induced confinement microscopy and single-particle imaging. Overall, our findings provide critical insights into how lipid-siRNA organization shapes LNP intracellular dynamics, offering rational design principles for optimizing LNP-based RNA therapeutics.

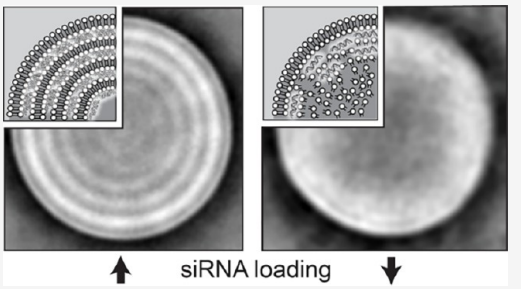

INTRODUCTION

Lipid nanoparticles (LNPs) have emerged as highly effective delivery systems for gene therapy,[1−3] as demonstrated by their clinical success in delivering therapeutic nucleic acids to patients, including siRNA (Onpattro, 2018),[4] mRNA (COVID vaccines, 2020),[5] and CRISPR gene-editing tools (Phase III, 2024).[6] Typically, LNPs are composed of ionizable lipids, helper lipids, cholesterol, and polyethylene glycol (PEG)-lipids. LNPs can exhibit diverse morphologies and internal structures depending on their lipid composition and nucleic acid cargo, as revealed by cryogenic electron microscopy (cryo-EM) studies.[7−12] Despite this, most LNP optimization efforts have focused on efficacy outcomes, such as target protein or mRNA expression levels, rather than the structural features that might drive the efficacy. While certain LNP structures correlate with enhanced RNA efficacy,[12−14] the underlying structure−function relationships, particularly how LNP structural organization influences intracellular dynamics before RNA cargo release, remain poorly understood. Moreover, structural studies often emphasize overall LNP morphology, with limited interpretation of the spatial organization of lipids and RNA within the nanoparticles. These subtle yet critical variations, though not always reflected in observable morphology, may significantly impact LNP intracellular performance. Thus, there is a pressing need for in-depth investigation into the detailed structural organization of LNPs and its connection to intracellular behavior beyond RNA efficacy alone.

Small interfering RNAs (siRNAs) are among the most extensively studied RNA cargos delivered by LNPs[15−17] and have led to FDA-approval of the first siRNA-loaded LNP drug, Onpattro, in 2018.[18] Unlike mRNA-LNPs, siRNA-loaded LNPs exhibit a more defined internal structure, as demonstrated by cryo-EM studies from several groups.[7,8,11,19] These studies have revealed that siRNA-LNPs form multilamellar concentric layers in the lumen at high siRNA payloads, whereas at lower payloads, they adopt an amorphous core structure. Additionally, it has been suggested that helper lipids migrate toward the LNP core at higher siRNA concentrations, whereas they preferentially localize near the LNP surface at lower concentrations. While these structural insights are valuable, their influence on LNP intracellular behavior remains largely unexplored. On the other hand, many studies on siRNA-LNP intracellular behavior have provided critical insights, significantly advancing our understanding of delivery mechanisms.[20−23] However, as these studies

Received: December 20, 2024
Revised: February 28, 2025
Accepted: March 3, 2025
Published: March 11, 2025

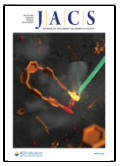

https://doi.org/10.1021/jacs.4c18308
J. Am. Chem. Soc. 2025, 147, 10430−10445

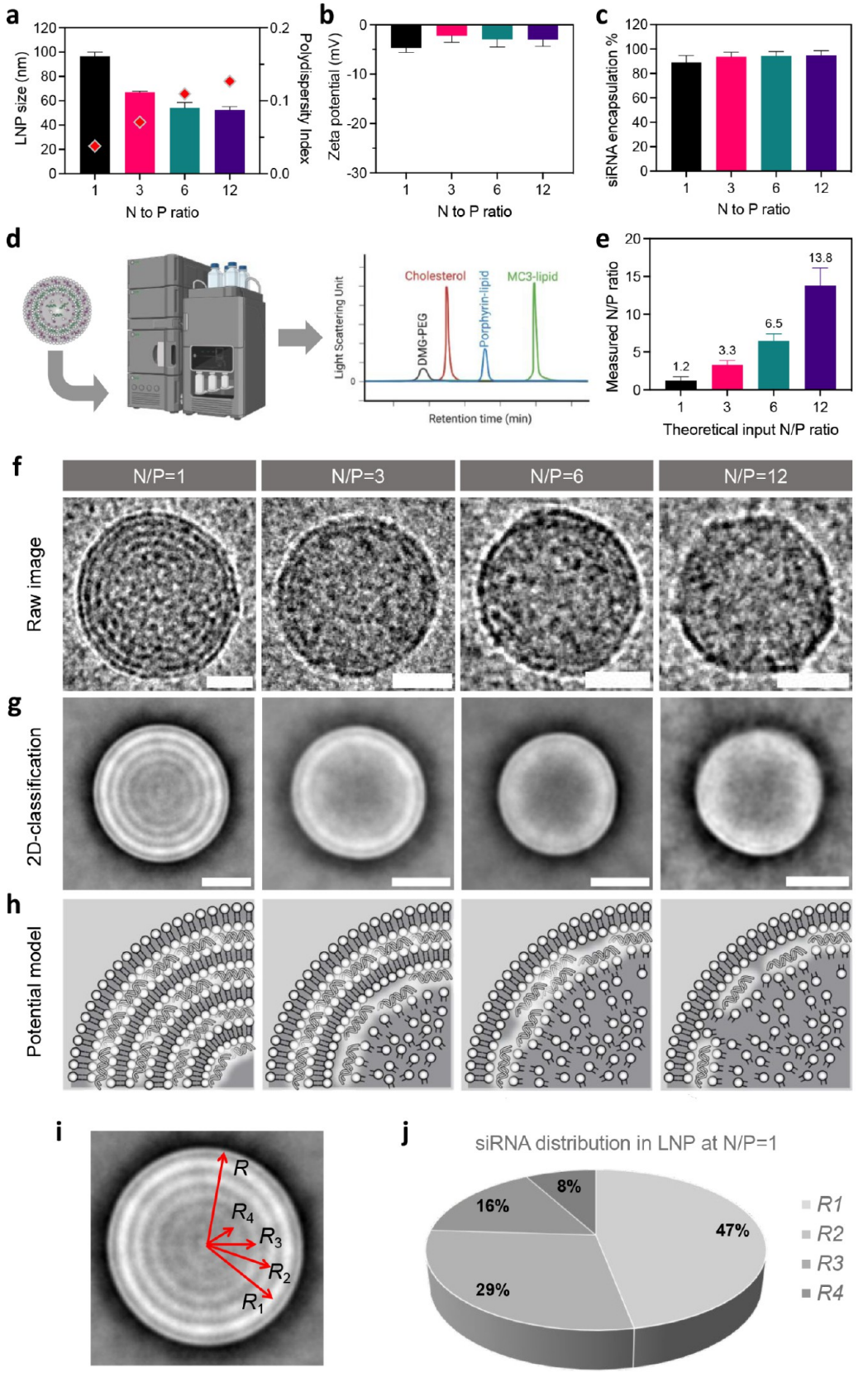

Figure 1. Synthesis and characterization of siRNA-LNPs at varying N/P ratios. (a) Size (measured by dynamic light scattering), (b) zeta potential and (c) siRNA encapsulation efficiency of LNPs. (d) Schematic illustration of lipid quantification using UPLC and the corresponding chromatogram. (e) Measured N/P values in synthesized LNPs. Data are presented as means ± standard deviation (n = 8). (f) Representative LNP from cryo-EM micrograph. (g) Select 2D classes for porphyrin-LNP at different N/P ratios. Scale bar = 25 nm. (h) Proposed siRNA organization in LNPs at varying N/P ratios. For simplicity of the illustration, DMG-PEG and cholesterol are not shown. (i, j) Calculated siRNA payload distribution within each concentric layer of LNP at N/P = 1 from the most outer (R_1) to inner (R_4).

https://doi.org/10.1021/jacs.4c18308
J. Am. Chem. Soc. 2025, 147, 10430−10445

are typically not designed to explore structure−function relationships, the understanding of observed intracellular delivery dynamics in relation to LNP structure remains limited.

Fluorescently labeled lipids are frequently used to track LNP distribution during intracellular uptake. Porphyrin-lipid is one such lipid that is both fluorescent and photoresponsive.[24−26] Additionally, it acts as a helper lipid, featuring the same phosphate headgroup as distearoyl-phosphatidylcholine (DSPC), the helper lipid component used in Onpattro formulations. This structural similarity makes porphyrin lipid an ideal substitute for maintaining the surface properties of comparable LNP formulations. Beyond its structural compatibility, porphyrin-lipid can also facilitate siRNA endosomal release upon light irradiation due to its photosensitizing properties.[27] This multifunctionality makes it a valuable tool for investigating how lipid-siRNA organization within LNPs influences the behavior of functional, stimuli-responsive lipids during intracellular trafficking, and may have downstream use in therapeutic release triggered by applied local fields.

In this study, we used porphyrin-lipid as a model helper lipid to synthesize siRNA-loaded LNPs based on the Onpattro formulation, investigating how variations in lipid-siRNA organization influence intracellular delivery dynamics. Lipid-siRNA organization was modulated by adjusting the nitrogen-to-phosphate (N/P) ratio, which reflects the molar ratio of nitrogen groups in ionizable lipids to phosphate groups in siRNA. We prepared siRNA-LNPs with N/P ratios of 1, 3, 6, and 12, representing a gradient from fewer to more helper lipids on the LNP surface. We used cryo-EM and photochemical analyses to reveal that helper lipid distribution to the LNP surface increased as siRNA loading decreased, whereas siRNA was consistently localized near the surface independent of siRNA concentration. The lipid-siRNA organization significantly altered the LNP's physical properties, such as membrane fluidity. During cellular uptake, LNPs with a higher density of porphyrin-lipids on their surface showed stronger binding and fusion with the cell membrane, enhancing both intracellular uptake and cytosolic siRNA delivery. Within endosomal compartments, the internal lipid-siRNA organization significantly affected helper lipid function in response to light stimulation, resulting in substantial differences in light-activated siRNA endosomal release. Single-particle imaging in solution, achieved using Convex Lens-induced Confinement (CLiC) microscopy,[19] further demonstrated that LNP dissociation upon light exposure was strongly dependent on lipid-siRNA organization. Overall, our study emphasizes the important role of lipid-siRNA organization in shaping the intracellular behavior of LNPs. These findings provide valuable insights into the structure−function relationship of LNPs and lay important groundwork for progress toward the rational design of LNP-based RNA therapeutics.

RESULTS

Synthesis and Characterization of siRNA-LNPs at Varying N/P Ratios. To investigate how lipid-siRNA organization affects intracellular delivery, we synthesized LNPs with N/P ratios of 1, 3, 6, and 12 (referred to as NP1 to NP12) using a standard microfluidic mixing method.[28] The LNPs consisted of MC3-lipid/Porphyrin-lipid/Cholesterol/DMG-PEG in a 50:10:38.5:1.5 molar ratio unless stated otherwise. Porphyrin-lipid was used as a model helper lipid and fluorescent marker to elucidate lipid-siRNA organization and to probe their intracellular dynamics. The structure and spectral properties of porphyrin-lipid are shown in Figure S1. Key characteristics, including particle size, zeta potential, and siRNA encapsulation efficiency, are presented in Figure 1a−c. As the N/P ratio increased, the average particle size decreased from 95 nm (NP1) to 50 nm (NP12), while the polydispersity index (PDI) increased modestly from 0.038 (NP1) to 0.127 (NP12), indicating a more heterogeneous size distribution. The average size reduction could be attributed to two factors: 1) At higher N/P ratios, the siRNA payload per LNP is reduced. 2) In LNPs with higher N/P ratios, more helper lipids are recruited to LNP surface rather than complexed in the lumen, increasing surface area and consequently reducing particle size. The zeta potential remained slightly negative and consistent across all formulations, and siRNA encapsulation efficiency exceeded 90%, indicating no significant loss in nucleic acid loading as the N/P ratio varied. To accurately quantify N/P ratios and ensure good quality control of synthesized LNPs, we developed an UPLC-ELS analysis pipeline. Lipid component concentrations, particularly MC3-lipid, were measured by UPLC (Figures 1dand S2), while siRNA contents in LNP was quantified using the Ribogreen assay. The measured N/P ratio was then calculated by integrating these two measurements. As shown in Figure 1e, the measured N/P ratios closely matched the theoretical input ratios, confirming the reproducibility and quality control of our LNP synthesis.

We then employed cryo-EM to visualize the internal structures of porphyrin-LNPs across varying N/P ratios. As shown in the micrographs (Figure 1f for individual particles and Figure S3 for larger views), LNPs at NP1 exhibited a well-defined multilamellar structure, consistent with previous reports on similar siRNA-LNP systems at NP1.[7,11] As the N/P ratio increased (i.e., with decreasing the siRNA payload), these lamellar structures became progressively less distinct, and the LNP surface appeared less spherical, particularly at NP12. Since individual micrographs offer limited statistical insight—a common challenge in cryo-EM imaging of LNPs—we improved our analysis by collecting hundreds of cryo-EM images per formulation. These images were processed using a machine learning algorithm to pick high-quality particles,[29] followed by 2D classification to align particles with same features. This process enabled averaging of particles with sufficiently similar diameters to enhance the internal detail of the overall LNP. The workflow is illustrated in Figure S4, and particle information is summarized in Table S1. A total of 6579, 5572, 8256, and 3734 high-quality particles were obtained for LNPs at N/P ratio from 1 to 12, respectively, and subjected to 2D-classification. In the 2D classification results, contrast was reversed from the original EM images, following standard cryo-EM convention: bright regions corresponded to stronger electron scattering, while darker regions represented weaker scattering.

As shown in Figures 1g and S5, the 2D classification of LNP at NP1 revealed a clear multilamellar structure, with a bright, thin outer rim likely representing the phosphate head groups of the helper lipids at the LNP surface. Internally, five concentric rings were visible, likely consisting of siRNA layers sandwiched between lipid bilayers, with electron scattering decreasing toward the center. At NP3, a single, well-defined inner ring appeared near to LNP surface, with diffuse bright signals extending into the amorphous core. As the N/P ratio increased to 6, the concentric ring that was prominent at NP3 became more ambiguous and diffuse. By NP12, no structured inner rings were visible, and the LNP lumen appeared fully amorphous. Given that stronger electron-scattering is attributed to the

https://doi.org/10.1021/jacs.4c18308
J. Am. Chem. Soc. 2025, 147, 10430−10445

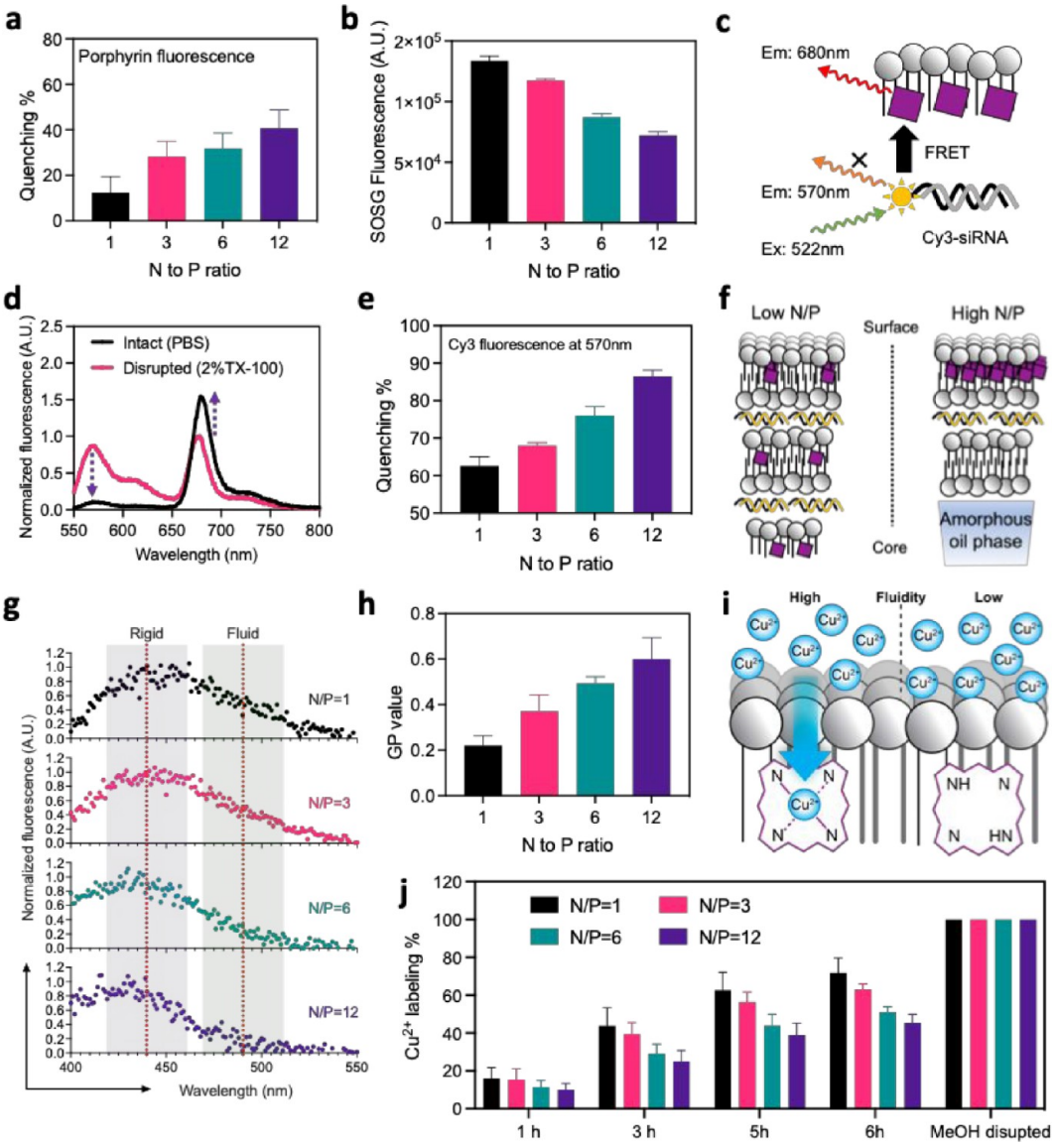

Figure 2. Validation of lipid-siRNA organization using photochemical techniques. (a) Porphyrin fluorescence quenching% and (b) SOSG fluorescence of 1%porphyrin-LNP at 1 μM porphyrin concentration at varying N/P ratio. Data are presented as means ± standard deviation (n = 3). (c) Schematic illustration of energy transfer between cy3-siRNA and porphyrin-lipid. (d) Fluorescence spectra (Ex: 522 nm) of intact and disrupted 1%porphyrin-LNPs when loaded with cy3-siRNA. (e) Cy3 fluorescence quenching% at 570 nm in intact 1% porphyrin-LNPs at varying N/P ratios. Conc. of cy3-siRNA = 200 nM. (f) Schematic illustration of varying helper lipids organization in LNPs at low and high N/P ratio. (g) Porphyrin-LNP (10% porphyrin-lipids) membrane fluidity measured by C-laurdan assay and the corresponding GP value (h), conc. of total lipid = 100 μM and conc. of C-laurdan = 10 μM. Data are presented as means ± standard deviation (n = 3). (i) Schematic illustration of Cu^{2+} chelation onto the porphyrin center within the LNP membrane, with higher membrane fluidity facilitating Cu^{2+} penetration. (j) Cu^{2+} chelation efficiency onto the porphyrin center after 1, 3, 5, 6 h of incubation at 35 °C in solution or following complete disruption by MeOH and further incubate 1 h after 5 h initial incubation. Data are shown as mean ± standard deviation (n = 3).

presence of siRNA (due to the negatively charged phosphate groups in the RNA backbones), these results suggest a model for siRNA organization within LNPs (Figure 1h): regardless of the siRNA payload, RNA tends to localize first near the LNP surface, filling inner spaces only after the surface region is saturated. At NP1, where siRNA is abundant, the RNA is well-organized between lipid bilayers. As the siRNA payload decreases, more of the LNP lumen becomes amorphous, providing siRNA with greater flexibility as the inner lipid layers lose their structure. This leads to a more diffuse, "cloudy" layer in LNPs at NP3 and NP6, following the well-defined ring. Interestingly, in LNPs with low siRNA loading (NP12), siRNA remains predominantly near the surface based on electron scattering pattern, rather than condensing into the amorphous core. This arrangement likely reduces the local negative charge density from siRNA and thus more favorable.

At NP1, where the siRNA saturates the LNP, we assume that the siRNA is evenly distributed across the concentric rings, though the outermost ring may have slightly higher siRNA density based on contrast differences. The amount of siRNA in each ring can be calculated as proportional to $4\pi R^2 \times \Delta r$, where R is the radius of the ring and Δr is the thickness occupied by the siRNA. As shown in Figure 1i,j, the LNP has a radius R of 32 nm, with radii for the concentric rings (R_1−R_4) measuring 28.70, 22.66, 17.08, and 11.77 nm, respectively. Based on these dimensions, the outermost ring contains 47% of the loaded

https://doi.org/10.1021/jacs.4c18308
J. Am. Chem. Soc. 2025, 147, 10430−10445

siRNA, with the inner layers containing 29%, 16%, and 8%, respectively. At N/P ratios higher than 1, a greater percentage of siRNA is expected to be located near the surface based on the contrast pattern, although the radial distribution may become more variable. This analysis of siRNA distribution in LNP reveals an important feature: unlike liposomal drugs, where the cargo is typically concentrated in the lumen, siRNA in the LNP system is predominantly organized near the surface (>50%). Collectively, these data confirm that by modulating the siRNA payload, we synthesized LNPs with distinct internal siRNA organizations, highlighting the significant impact of siRNA loading on LNP internal structure.

Characterization of Lipid-siRNA Organization Using Photochemical Techniques. In prior work, cryo-EM measurements provided insights into the morphology and siRNA organization within LNPs at varying N/P ratios, while the spatial distribution of helper lipids remained unclear. To address this, we leveraged the fluorescent properties of porphyrin-lipids to probe their arrangement. As shown in Figure 2, porphyrin-lipid fluorescence exhibited stronger quenching in LNPs with higher N/P ratios. Additionally, we assessed the capacity of porphyrin-lipids to generate singlet oxygen upon exposure to 670 nm light. As the N/P ratios increased, singlet oxygen production decreased (Figure 2b), consistent with the fluorescence quenching. Both results indicate tighter lipid packing at higher N/P ratios, supporting the enrichment of helper lipids at the LNP membrane. Next, we employed fluorescence resonance energy transfer (FRET) to explore the interaction between siRNA and helper lipids (Figure 2c–e). Cy3-labeled siRNA was loaded into the porphyrin-LNPs containing 1% porphyrin-lipid. To ensure consistent Cy3 fluorescence across all N/P ratios, a fixed amount of Cy3-siRNA was loaded into the LNP formulations, with nonlabeled siRNA added to achieve the desired N/P ratio. It was also confirmed that Cy3-siRNA itself does not cause fluorescence self-quenching (Figure S6). Due to the overlap between Cy3's emission and porphyrin-lipid's absorbance (Figure S7), FRET occurred when the two dye molecules were in close proximity (Figure 2c). As shown in Figure 2d, when excited at 522 nm, intact porphyrin-LNPs exhibited weak Cy3 fluorescence at 570 nm and a strong, characteristic porphyrin emission at 680 nm. Upon LNP disruption, Cy3 fluorescence was restored, and porphyrin emission significantly decreased, confirming that FRET occurred between Cy3-siRNA and the porphyrin-lipid in intact LNPs. Increasing the N/P ratio resulted in greater quenching of the Cy3 fluorescence signal at 570 nm (Figure 2e), suggesting that the siRNA and porphyrin-lipids were in closer proximity at higher N/P ratios. This result aligns with the cryo-EM findings, which showed that siRNA, regardless of loading ratio, localized near the LNP surface. It also supports the trend of helper lipids migrating to the surface as N/P ratios increased. A model is illustrated in Figure 2f: at lower N/P ratios, siRNA and porphyrin-lipids were more evenly distributed throughout the LNP, resulting in greater spatial separation and less FRET. In contrast, at higher N/P ratios, both components concentrated near the surface, reducing their separation and thus increasing FRET-induced Cy3 fluorescence quenching.

We next examined the membrane fluidity of porphyrin-LNPs at varying N/P ratios using the C-Laurdan assay, which measures lipid packing and the polarity of the membrane environment.[30] C-Laurdan integrates into the lipid bilayer and shifts its emission wavelength based on membrane fluidity—toward shorter wavelengths in rigid membranes, and toward longer wavelengths in fluid ones. This spectral shift is quantified by the generalized polarization (GP) value, ranging from −1 to 1, with higher value corresponding to greater membrane rigidity. As shown in Figure 2g,h, increasing the N/P ratio in porphyrin-LNPs led to higher membrane rigidity, as GP values increased from 0.22 (NP1) to 0.60 (NP12). This again supports that higher N/P ratios promote migration of helper lipids to the LNP surface. The bulky porphyrin ring on the lipid side chain, capable of forming $\pi-\pi$ stacking, likely contributes to the increased rigidity of LNP membranes at higher N/P ratios. In contrast, MC3-LNPs, which use DSPC as the helper lipid, showed consistently low GP values (close to 0) across all N/P ratios (Figure S8), indicating a more fluid membrane compared to porphyrin-LNPs. While no significant GP changes were observed in MC3-LNPs across N/P ratios, this does not necessarily imply that DSPC distribution within the membrane remains constant. Previous studies have shown that altering the lipid-to-cholesterol ratio in saturated lipid membranes like DSPC and DPPC induces changes in membrane fluidity. This change is detectable through atomic force microscopy but not by Laurdan fluorescence spectral shifts and GP values, likely due to assay's sensitivity limitations.[31]

Next, we employed an independent method to assess LNP membrane fluidity, taking advantage of the porphyrin-lipid's metal-chelating properties.[32−34] Porphyrin-LNPs were incubated with an excess of Cu^{2+} (eq: 3500) in solution (Figure 2i), as a more fluid lipid membrane would allow greater Cu^{2+} penetration into the lipid tail region, facilitating more efficient chelation with the porphyrin macrocycle. This chelation induces a blue shift in the porphyrin Q-band absorbance from 666 nm (unchelated) to 653 nm (chelated) (Figure S9) and UPLC chromatography was able to differentiate the chelated and unchelated populations based on their elution time (Figure S10). As shown in Figures 2j and S11, increasing the N/P ratio resulted in a slower Cu^{2+} chelation rate, indicating reduced membrane fluidity. While extended incubation times increased Cu^{2+} chelation across all N/P ratios, the overall trend of slower chelation at higher N/P ratios persisted. After 5 h of incubation, LNPs with NP1 showed a Cu^{2+} chelation efficiency of 62.6%, while LNPs with NP12 reached only 38.9%. Further incubation (up to 6 h) led to minimal additional increases in chelation efficiency, suggesting the reaction had reached equilibrium. In contrast, further incubation in a methanol disruption condition (all samples after 5h incubation were diluted with methanol to force LNPs disrupted and incubated for an additional hour) led to 100% Cu^{2+} chelation efficiency for LNPs across all N/P ratio, confirming that the initial differences were indeed attributed to variations in membrane fluidity and Cu^{2+} accessibility to the porphyrin ring.

Overall, using various photochemical techniques, we systemically investigated the lipid-siRNA organization and the distribution of helper lipids within LNPs. As the N/P ratio increased, more helper lipids migrated to the LNP surface, leading to decreased membrane fluidity.

Lipid-siRNA Organization Modulates LNP Fusion with the Cell Membrane. Our experiments have helped establish two important insights regarding lipid-siRNA organization in LNPs at varying N/P ratios: 1) helper lipids become enriched at the LNP surface at higher N/P ratios, and 2) siRNA consistently localizes near the LNP membrane, regardless of the siRNA payload amount, under the wide range of conditions studied here. We next investigated how these organizational differences influence LNP intracellular trafficking. Using porphyrin-lipid as

https://doi.org/10.1021/jacs.4c18308
J. Am. Chem. Soc. 2025, 147, 10430−10445

a fluorescent helper lipid tracer, porphyrin-LNPs containing FAM-labeled siRNA were incubated with PC3-Luc6 cells, and their intracellular delivery was imaged via confocal microscopy. As shown in Figure 3a, increasing the N/P ratio resulted in

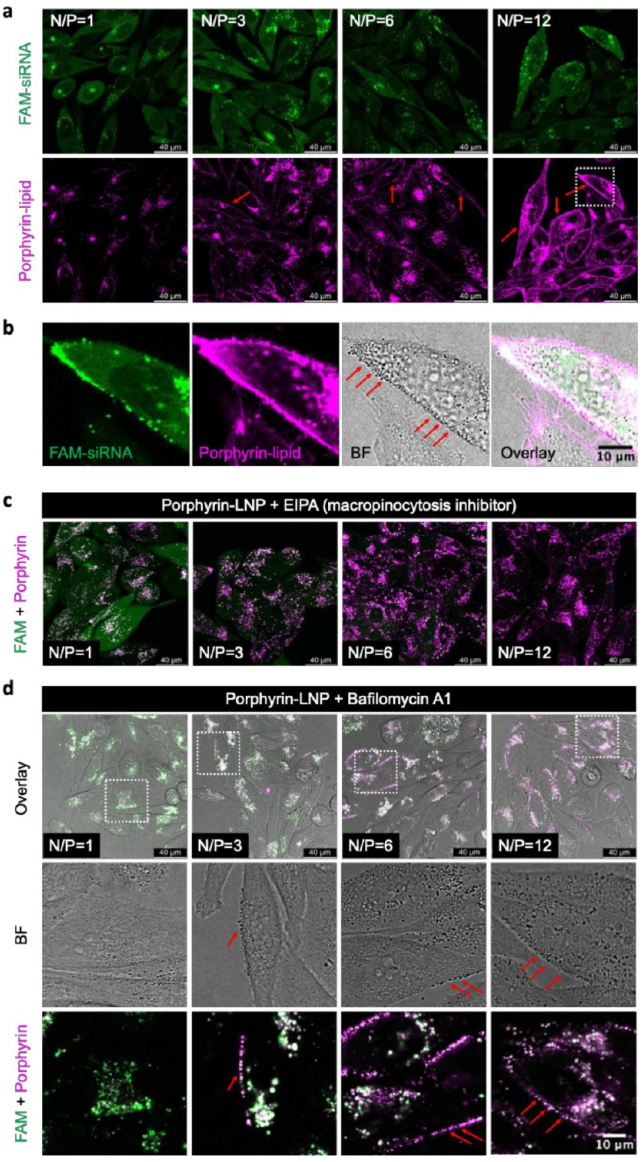

Figure 3. Lipid-siRNA organization impacts LNP cellular uptake pathway. (a) Confocal microscopy images of PC3-Luc6 cells after porphyrin-LNP uptake for 6 h at a porphyrin concentration of 2 μM. Stronger binding of LNP lipids to cell outer membrane was observed as N/P ratio increases, indicated by red arrows. (b) Zoom-in view of dashed square in (a). Vesicular structures were observed on cell outer membrane from the bright field image. (c) LNP uptake at same condition as in (a), in the presence of EIPA (50 μM) as inhibitor. (d) LNP uptake at same condition as in (a), in the presence of bafilomycin A1 (1 μM) as inhibitor.

significantly stronger porphyrin-lipid fluorescence on the cell membrane. For NP1, porphyrin-lipid fluorescence appeared primarily in punctate patterns within intracellular organelles, whereas for NP12, fluorescence was observed both intracellularly and on the cell membrane, suggesting that a portion of LNP may have fused with the membrane. Interestingly, porphyrin-lipid fusion remained in the absence of siRNA cargo (Figure S12). Empty porphyrin-LNPs exhibited similarly strong membrane fusion as NP12, indicating that the fusion is related to changes in LNP surface properties, driven by lipid-siRNA organization as the N/P ratio increases. Brightfield images (Figure 3b) further revealed vesicular structures forming on the cell membrane in regions with strong porphyrin fluorescence, supporting LNP binding and potential membrane fusion. These vesicles, which occasionally contained FAM-siRNA signal, may represent different stages of the membrane fusion. In vesicles with only porphyrin fluorescence, the FAM-siRNA may have already been released into the cytosol following LNP fusion. Notably, despite the lower FAM-siRNA concentration in LNPs at high N/P, some cells exhibited comparable cytosolic siRNA signals to those in LNPs at low N/P. Specifically, the average FAM intensity in the cytosol was 26.7 for NP1 and 26.3 for NP12 (Figure S13), suggesting enhanced cytosolic siRNA delivery at high N/P ratios. This observation aligns with cryo-EM data showing that siRNA localizes primarily near the LNP surface, increasing the likelihood of siRNA release when helper lipids fuse with the cell membrane and peel away. Similar enhanced membrane fusion was also observed in KB cells (Figure S14), indicating that this may be a general trend driven by changes in lipid-siRNA organization.

To investigate the uptake pathway involved in LNP-membrane fusion, we applied a range of uptake inhibitors. Previous studies have reported that LNP endocytosis occurs primarily through clathrin-mediated pathways and macropinocytosis.[21] Given that the vesicular structures observed on the cell membrane could be associated with membrane ruffling—a hallmark of macropinocytosis[35]—we first applied the macropinocytosis inhibitor 5-(*N*-ethyl-*N*-isopropyl)-Amiloride (EIPA). EIPA blocks Na^+/H^+ exchangers, which are crucial for all forms of macropinocytosis.[36] As shown in Figure 3c, LNPs treated with EIPA exhibited significantly reduced porphyrin fluorescence on the cell membrane across all N/P ratios compared to untreated samples (Figure 3a). Even at the highest N/P ratio of 12, only faint membrane fluorescence was detected. Additionally, cytosolic FAM-siRNA signal was significantly reduced for LNPs at N/P ratios of 3, 6, and 12, but remained strong for NP1 LNPs (Figures 3c and S15). Since membrane fusion likely facilitates cytosolic delivery of FAM-siRNA, the macropinocytosis inhibitor blocked this process, resulting in reduced cytosolic FAM-siRNA levels in LNPs at N/P ratio of 3, 6, and 12 compared to their culture under normal conditions. Next, we tested clathrin-mediated endocytosis using its inhibitor, chlorpromazine (CPZ).[37] As shown in Figure S16, CPZ modestly reduced membrane porphyrin fluorescence, yet the cytosolic FAM-siRNA signal remained largely unchanged across N/P ratios, indicating clathrin-mediated uptake has a less prominent role in the endocytosis of porphyrin-LNP. Together, these results suggest that the fusion between porphyrin-lipids and the cell membrane is closely linked to macropinocytosis. The unique membrane properties of these LNPs, such as increased rigidity from changes in lipid-siRNA organization, appear to trigger fusion during the macropinocytosis process, though further investigation is required to fully understand the mechanism.

In addition to direct fusion between LNP and cell outer membranes, porphyrin-lipid fluorescence observed at the cell surface may also result from LNP exocytosis following intracellular uptake. During exocytosis, multivesicular bodies containing LNP can fuse with plasma membrane.[38] Notably, it has been reported that approximately 70% of siRNA-lipid complexes can undergo exocytosis after LNP uptake,[39]

https://doi.org/10.1021/jacs.4c18308
J. Am. Chem. Soc. 2025, 147, 10430−10445

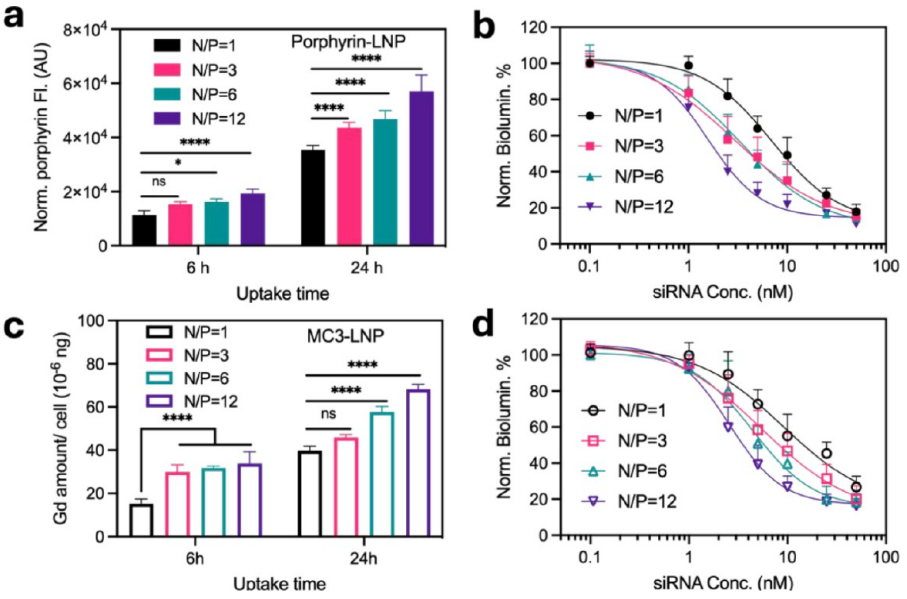

Figure 4. Lipid-siRNA organization impacts LNP intracellular uptake amount and siRNA knockdown efficacy. (a) porphyrin-LNP cellular uptake amount in PC3-Luc6 cells after 6 and 24 h incubation at total lipid concentration of 12 μM (porphyrin of 2 μM). The porphyrin fluorescence was measured after the cells were fully digested by DMSO. (b) Normalized bioluminescence from PC3-Luc6 cells after treated with porphyrin-LNP-siLuc at varying N/P ratios and doses for 24 h. (c) MC3-LNP cellular uptake amount based on Gd^{3+} in PC3-Luc6 cells after 6 and 24 h incubation at a total lipid concentration of 12 μM. (d) Normalized bioluminescence from PC3-Luc6 cells after treated with MC3-LNP-siLuc at varying N/P ratios and doses for 24 h. All the data are presented as means ± standard deviation (n = 3). For (a) and (c), data were analyzed through a two-way ANOVA, ****$p < 0.0001$, *$p < 0.05$.

potentially also contributing to the accumulation of lipid signals on the cell membrane. To investigate this possibility, we used bafilomycin A1 (BafA1), a potent inhibitor of endosomal acidification that blocks the vacuolar-type H^+-ATPase (V-ATPase) proton pump,[40] preventing acidification of intracellular compartments such as endosomes and lysosomes. Without acidification, these organelles are trapped in the early stages of endocytosis and cannot undergo endocytic recycling. As shown in Figure 3d, in the presence of BafA1 inhibition, LNP treated cells exhibited almost no cytosolic FAM-siRNA signal, highlighting that endosomal acidification is critical for siRNA endosomal escape. This aligns with prior knowledge that ionizable lipids in LNPs must be protonated in acidic environments to fuse with the endosomal membrane and release RNA cargos into the cytosol. Interestingly, despite BafA1 treatment, LNPs with higher N/P ratios still showed vesicular structures on the cell membrane, while NP1 LNPs displayed no membrane binding. This suggests that LNP-cell membrane fusion occurs upon initial contact, rather than as a result of endocytic recycling and lipid redistribution. Notably, BafA1 can also impair macropinocytosis, as both macropinocytosis initiation and maturation are reported to require V-ATPase and acidification.[41−43] Therefore, BafA1-treated cells exhibited reduced membrane binding compared to untreated cells, as shown in Figure 3a.

To determine whether porphyrin-LNP uptake and membrane fusion occurs via an active or passive mechanism, we evaluated their intracellular uptake at 37 and 4 °C (Figure S17). Almost no LNP uptake was observed at 4 °C, suggesting that the uptake of porphyrin-LNPs is largely energy-dependent rather than driven by passive diffusion. To further confirm this, we performed an ATP depletion study by preincubating cells with sodium azide (NaN_3) and 2-Deoxy-D-glucose (2-DG)[44] before exposure to porphyrin-LNP (Figure S18). Under these ATP-depleted conditions, minimal fluorescence was detected, reinforcing that porphyrin-LNP uptake and membrane fusion relies on active transport.

Collectively, these data demonstrate that lipid-siRNA organization significantly influences LNP intracellular uptake dynamics. Higher N/P ratios, which enrich helper lipids at the LNP surface, promote membrane fusion and facilitate cytosolic siRNA delivery. Inhibitor studies confirmed that this fusion occurs upon initial contact, likely through the macropinocytosis pathway, underscoring the importance of lipid organization in optimizing RNA delivery systems.

Lipid-siRNA Organization Impacts LNP Cellular Uptake and siRNA Efficacy. Next, we conducted quantitative intracellular uptake experiments to examine how lipid organization in LNPs affects uptake levels. For porphyrin-LNP, we leveraged the inherent fluorescence of porphyrin-lipids to quantify their uptake, with cells fully digested by DMSO to completely unquench the porphyrin fluorescence signal. For MC3-LNP, which lacks a fluorescent lipid label, 2% DTPA-BSA(Gd) lipid was incorporated into the LNP formulation, allowing for Gd^{3+} quantification by inductively coupled plasma mass spectrometry (ICP-MS) as an indicator of total lipid uptake. As shown in Figure 4a,c, both porphyrin-LNPs and MC3-LNPs showed increased intracellular uptake in PC3-Luc6 cells as the N/P ratio increased, regardless of whether porphyrin-lipid or DSPC was used as the helper lipid. This suggests that changes in lipid organization—specifically, the enrichment of helper lipids on the LNP surface at lower siRNA payloads—may enhance LNP uptake. The changes in lipid organization alter LNP surface properties, such as increased rigidity, which may promote uptake via pathway like macropinocytosis, as indicated by our confocal imaging results (Figure 3a−c). Additionally, it is reported that LNP surface chemistry impacts the composition of formed protein corona, which in turn affects cellular uptake.[45,46] Therefore, surface property changes resulted from lipid-RNA organization could also alter LNP interactions with specific

https://doi.org/10.1021/jacs.4c18308
J. Am. Chem. Soc. 2025, 147, 10430−10445

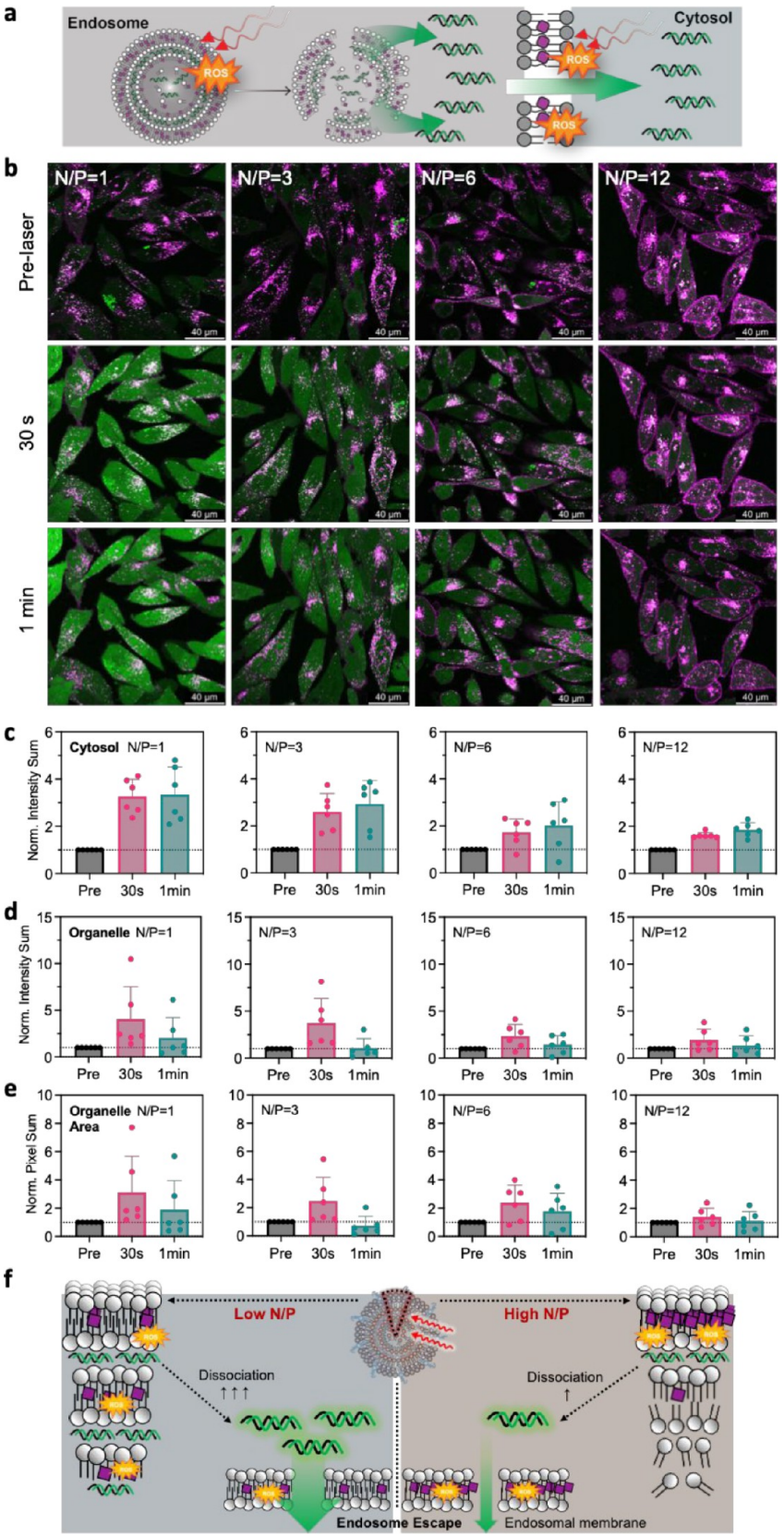

Figure 5. Lipid-siRNA organization impacts light-activated siRNA endosomal escape. (a) Schematic of light-activated siRNA endosomal escape by porphyrin lipid nanoparticles: after endocytosis, some porphyrin-lipids translocate to the endosomal membrane. Upon near-infrared light exposure, they generate reactive oxygen species (ROS), inducing LNP dissociation to release siRNA into the endosomal lumen and disrupting the endosomal membrane, ultimately releasing siRNA into the cytosol. (b) Confocal microscopy images of PC3-Luc6 after treatment with porphyrin-LNPs (FAM-siRNA) at varying N/P ratios for 6 h. LNPs with lower N/P ratio exhibited stronger FAM-siRNA endosomal escape into the cytosols post light irradiation at 660 nm for 30s and 1 min, respectively. (c, -d) Quantification of FAM fluorescent signal intensity sum in cytosol (c) and organelles (d)

https://doi.org/10.1021/jacs.4c18308
J. Am. Chem. Soc. 2025, 147, 10430−10445

Figure 5. continued

before and after light exposure. (e) Quantification of organelle area change before and after light exposure. All the data are presented as means ± standard deviation (n = 6 cells). (f) Proposed mechanism on how lipid-siRNA organization impacts LNP dissociation and siRNA endosomal escape upon light activation. In porphyrin-LNPs with lower N/P ratios, porphyrin-lipids are more evenly distributed throughout the entire LNP. Upon light activation, this lipid organization promotes ROS across the LNP, enhancing LNP dissociation and facilitating substantial siRNA release into the endosomal lumen, primed for subsequent endosomal escape. Conversely, in porphyrin-LNPs with higher N/P ratios, porphyrin-lipids are concentrated in the membrane, leading to spatially restricted ROS generation. This restriction results in less efficient LNP dissociation, reduced siRNA release, and limited endosomal escape.

serum proteins, leading to variations in uptake. Notably, the same trend was observed across different helper lipids, which may represent a general phenomenon applicable to various LNP formulations.

Next, we investigated how lipid organization in LNPs affects siRNA knockdown efficacy. As shown in Figure 4b,d, LNPs with higher N/P ratios also exhibited enhanced siRNA knockdown efficacy against the luciferase gene, even at the same siRNA dose. The factors that lead to this observation are discussed as follows: ionizable lipids have traditionally been considered the primary factor driving differences in siRNA efficacy by facilitating endosomal membrane disruption.[47] For instance, at higher N/P ratios, excess ionizable lipids not complexed with siRNA may be protonated in acidic organelles, promoting endosomal escape. However, our results suggest that lipid-siRNA organization is equally important. Three key findings indicate that lipid-siRNA organization also contributes to siRNA efficacy. 1) At higher N/P ratios, increased LNP uptake (Figure 4a,c) results in greater siRNA delivery per cell, improving knockdown efficacy independent of endosomal escape. 2) Changes in lipid-siRNA organization can alter LNP uptake pathways, promoting direct fusion with the cell membrane (Figure 3a), thereby improving cytosolic siRNA delivery and efficacy. 3) siRNA preferentially localizes near the LNP surface (Figure 1g–j), especially at higher N/P ratios, which increases the chance of siRNA release into endosomal organelles upon LNP dissociation. In contrast, at lower N/P ratios, more siRNA remains encapsulated in the LNP core, making it harder to release and ultimately reducing knockdown efficacy. Altogether, these findings highlight the important role of lipid-siRNA organization in LNP design, as it impacts multiple stages of intracellular trafficking and ultimately influences siRNA efficacy. Ionizable lipids, while important, may not be the only factor determining the therapeutic effectiveness of RNA delivery.

Lipid-siRNA Organization Regulates Intracellular Lipid Functionality Upon Light Activation. After exploring the impact of lipid-siRNA organization during the initial cell interaction, we next examined how it affects LNP behavior during endocytosis, with a focus on endosomal escape, a critical barrier to RNA efficacy. One strategy to enhance LNP endosomal escape is the use of external stimuli, such as light, to trigger endosomal membrane disruption. We previously developed a method called "Light-Activated siRNA Endosomal Release" (LASER) using porphyrin-lipid nanoparticles (Figure 5a).[27] After LNP endocytosis and partial dissociation, some porphyrin-lipids can translocate to the endosomal membrane. Upon light activation, they generate membrane-specific reactive oxygen species (ROS), which can disrupt the endosomal membranes and allow trapped siRNA to be released into the cytosol.

Here, LASER was used as a tool to investigate and demonstrate through dynamic imaging on how lipid-siRNA organization affects the performance of functional lipid during LNP intracellular uptake. To account for fluorescence differences, FAM-siRNA loading was kept constant across N/P ratios, while unlabeled siRNA was added to low N/P ratio LNPs to achieve the desired ratio. As shown in Figure 5b, after 6 h of uptake, both FAM-siRNA and porphyrin fluorescence appeared in punctate patterns, with weak FAM signals in the cytosol (pre-laser). Following 30 s of light irradiation, NP1 LNPs showed the strongest siRNA endosomal escape, with the brightest FAM-siRNA signal observed in the cytosol. As the N/P ratio increased, cytosolic FAM intensity decreased. Quantification of FAM intensity in the cytosol (Figure 5c) showed that post-irradiation levels were 3.26-, 2.60-, 1.73-, and 1.62-fold of pre-irradiation levels for NP1, NP3, NP6, and NP12, respectively. Given that all N/P ratios had equal FAM-siRNA loading, these results confirm greater siRNA endosomal escape in low N/P LNPs following light activation.

Additionally, we observed a "light-up then decay" pattern of FAM signal within organelles after 30 s and 1 min of light exposure compared to pre-laser condition, particularly at lower N/P ratios: as shown in Figure 5d, the relative fold change in FAM intensity within organelles between 30 s and 1 min decreased from 4.04-fold to 2.02 (NP1), 3.74 to 1.05 (NP3), 2.34 to 1.43 (NP6), and 1.93 to 1.35 (NP12). Similar trends were observed in organelle area (Figure 5e), suggesting a two-step process for siRNA endosomal release: initially, light irradiation induces LNP dissociation, releasing siRNA into the endosomal lumen and activating FAM-siRNA fluorescence due to relief from self-quenching and FRET-induced quenching (with a FAM fluorescence spike observed in organelles at 30s). Subsequently, the endosomal membrane is disrupted, allowing FAM-siRNA to escape into the cytosol, resulting in a marked decline in organelle-associated FAM fluorescence by 1 min. The marked differences in FAM-siRNA endosomal escape across N/P ratios upon light irradiation can be explained by variations in lipid-siRNA organization. Our cryo-EM and photochemical data have revealed that at low N/P ratios, porphyrin-lipids are distributed throughout the LNP membrane and lumen, while at high N/P ratios, they concentrate primarily on the LNP surface (Figures 1f–h, 2a–f). Such structural differences suggest that LNPs at different N/P ratios respond differently to light irradiation (Figure 5f): at lower N/P ratios, with a more diffuse porphyrin-lipid distribution, LNPs generate higher amounts of ROS (Figure 2b) throughout the whole particle. Conversely, at high N/P ratios, porphyrin-lipid enrichment at the LNP surface leads to more localized and limited ROS generation (Figure 2b). ROS has been reported to induce drug release from liposomes by oxidizing unsaturated lipid bonds,[48] which disrupts particle integrity. In LNPs, ROS may react with the unsaturated MC3-lipid tails, inducing lipid conformational changes that promote LNP dissociation. Since MC3-lipids are situated mostly in the inner concentric layers complexed with siRNA or within the LNP lumen, low N/P LNPs present a higher likelihood of ROS interacting with MC3-lipids, resulting in stronger LNP

https://doi.org/10.1021/jacs.4c18308
J. Am. Chem. Soc. 2025, 147, 10430–10445

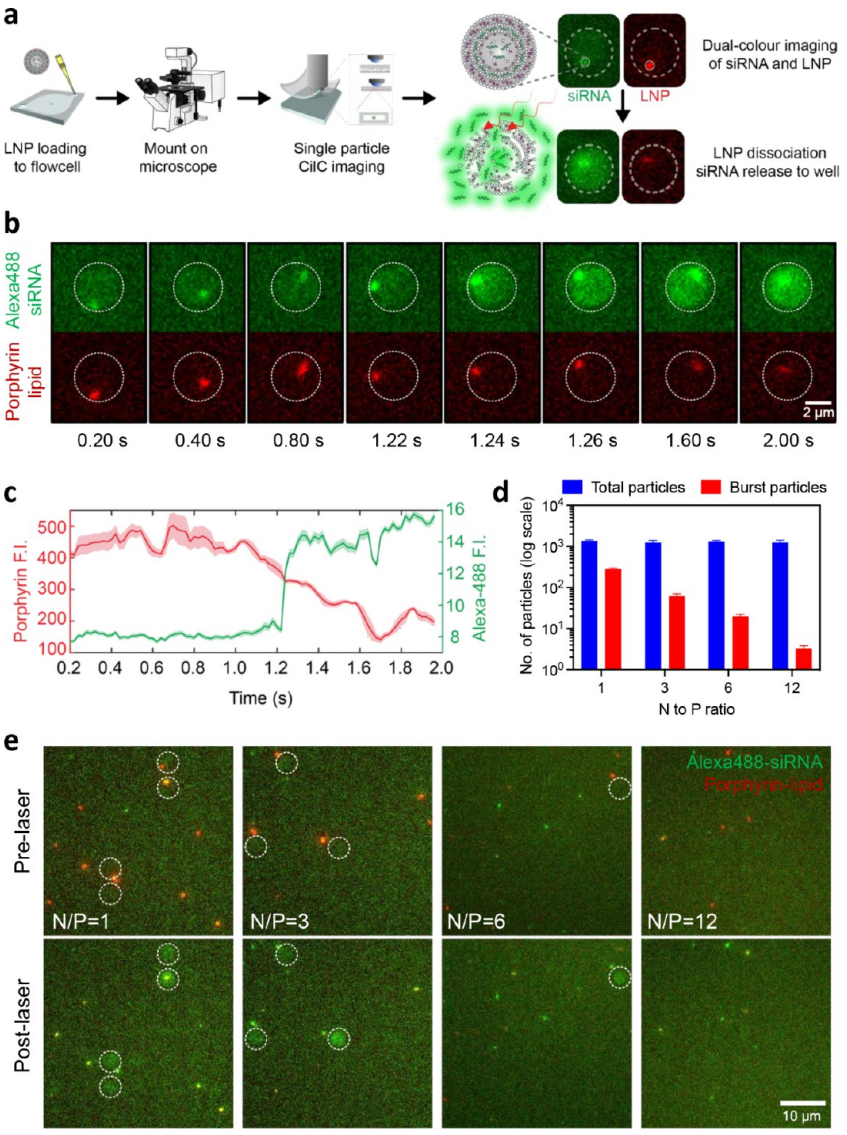

Figure 6. CLiC measurements of LNP dissociation and siRNA release upon light activation. (a) Schematic of Convex Lens-induced Confinement (CLiC) single particle imaging for visualization of siRNA release from light-activated LNPs. (b,c) Real-time imaging of light activated siRNA release from individual particles. (b) Timelapse imaging of Alexa488-siRNA (green) and porphyrin-lipid fluorescence (red). (c) Average fluorescence intensities from a single well (shown in b) over acquisition time (100 frames, 20 ms exposure time each) for both siRNA and porphyrin channels. (d) Bar graph showing the total number of particles and burst particles as a function of N/P ratios after 40 s of 647 nm laser exposure. (e) Pre- and post-laser images (overlay of siRNA and LNP fluorescence) of microwell arrays showing siRNA release from burst particles (circles with dashed lines) at different N/P ratios. Overall, burst events and siRNA release reduces as the N/P ratio increases.

dissociation and enhanced siRNA availability for subsequent endosomal release. The enhanced LNP dissociation at lower N/P ratios, as compared to higher ratios, is indicated by a more pronounced FAM fluorescence spike in endosomes (Figure 5d,e), prior to siRNA release into the cytosol (Figure 5b,c). Once siRNA enters the endosomal lumen, the next step is endosomal escape. As shown in Figure S19, porphyrin-lipid translocation to the endosomal membrane is substantial across all N/P ratios, evident by distinct porphyrin fluorescence localized on organelle membranes. This observation confirms LNPs at all N/P ratios can generate membrane-specific ROS to facilitate siRNA escape. These findings imply that the marked differences in FAM-siRNA endosomal escape upon light (Figure 5b) primarily arise from variations in siRNA availability within the endosomal lumen, rather than from the efficiency of the escape step itself. In summary, results in this section highlight the critical role of lipid-siRNA organization in determining the performance of functional lipid during the intracellular uptake, particularly when such functionality is spatially dependent.

Lipid-siRNA Organization Impacts Light-Activated LNP Dissociation. Intracellular imaging of porphyrin-LNP suggests that LNPs may undergo varying levels of dissociation upon light irradiation, influenced by lipid-siRNA structural organization. However, this observation is limited by the aggregate effect of numerous LNP particles within cells, providing only indirect evidence of individual LNP behavior under light exposure. To further investigate how lipid-siRNA organization influences LNP responsiveness to external stimuli and to provide direct evidence of light-induced LNP dissociation, we used Convex Lens-induced Confinement (CLiC) microscopy to visualize structural changes at the single-particle resolution level. The CLiC platform enables the

https://doi.org/10.1021/jacs.4c18308
J. Am. Chem. Soc. 2025, 147, 10430−10445

imaging and analysis of individual LNP particles under applied light fields.[19,49] As shown in Figure 6a, porphyrin-LNPs containing Alexa488-labeled siRNA were loaded into a custom microfluidic CLiC flow cell and visualized by CLiC microscopy (detailed in the Methods section). A 50 μL of LNP suspension was confined and trapped in an array of microwells (3-μm diameter, 500 nm depth) with the concentration optimized to ensure an average of one LNP particle per well, each appearing as a diffraction-limited spot (Figure 6a). The diffusion behavior of individual LNP particles was continuously monitored by simultaneously tracking fluorescence from both siRNA and porphyrin-lipid. Upon 647 nm excitation of the porphyrin-lipid, LNP dissociation could be triggered, releasing the siRNA, which would then diffuse and move rapidly within the microwell. As shown in Figure 6b,c, when LNPs at N/P ratio of 1 were excited simultaneously with both 488 and 647 nm light, fluorescence from Alexa488-siRNA (green) and porphyrin-lipid (red) initially appeared as a single, colocalized spot, representing an intact, freely diffusing LNP. Over time, continuous light irradiation caused the Alexa488 fluorescence to diffuse, filling the well by ∼1.24 s, with the average fluorescence intensity increasing from 8 to 16 photons per well. Simultaneously, porphyrin fluorescence decreased from 400 to ∼200 photons per well and became more diffuse. These data indicate that upon light exposure, LNPs dissociated, releasing encapsulated siRNA into the surrounding environment, which activates their fluorescence. We then compared the frequency of LNP burst events across N/P ratios (Figure 6d,e and Videos S1−S4): Approximately 1300 single particles were analyzed for each N/P ratio per experiment. The percentage of burst particles was 20.60%, 5.00%, 1.52%, and 0.27% for NP1, NP3, NP6, and NP12, respectively. NP1 exhibited 76.9 times more burst events compared to NP12, with only an average of 3.3 burst particles out of ∼1300 for NP12.

These single-particle CLiC imaging data provide direct visualization of individual LNP behavior upon light irradiation, clearly demonstrating that porphyrin-LNPs at lower N/P ratios are more prone to bursting under light exposure, indicative of stronger LNP dissociation and subsequent siRNA release. Dissociation differences across N/P ratios can be attributed to variations in porphyrin-lipid spatial distribution (Figure 5f). Moreover, the CLiC imaging data aligns well with prior intracellular imaging observations (Figure 5d,e), where LNPs with lower N/P ratios exhibited stronger initial siRNA fluorescence activation in organelles upon light exposure, followed by a subsequent fluorescence decrease—a "light-up then decay" pattern. The single-particle CLiC imaging data support that the "light-up" phase observed in intracellular imaging is due to LNP dissociation. Consequently, LNPs at lower N/P ratio would have more free siRNA available in the endosomal lumen, contributing to stronger subsequent siRNA escape from endosome into the cytosol.

Collectively, the single-particle imaging data support the claim that lipid-siRNA organization determines the extent of LNP dissociation upon light irradiation, highlighting the critical but often overlooked role of LNP dissociation in facilitating RNA endosomal escape. This important insight may be used in designing advanced therapeutics for controlled release.

DISCUSSION

LNP-based RNA therapeutics have advanced rapidly, yet our understanding of their intracellular dynamics, aside from RNA efficacy, remains limited, which hinders the rational optimization of LNPs. In this study, we provide key insights into how lipid-siRNA organization within LNPs can influence their intracellular delivery dynamics. Using cryo-EM and photochemical assays, we demonstrated how variations in siRNA loading (N/P ratio) affect the spatial distribution of lipids and siRNA. Cryo-EM analysis, including 2D classification of over 3500 particles per formulation, revealed unprecedented detail of siRNA-LNP structures, confirming that siRNA tends to localize near the LNP surface. Photochemical assays revealed that as siRNA loading decreased, helper lipids were enriched at the LNP surface. Confocal and CLiC microscopy further showed how lipid-siRNA organization impacts LNP intracellular delivery, dissociation, responsiveness to stimuli, and overall siRNA efficacy, providing valuable insights for LNP design.

Our findings extend beyond siRNA-loaded LNP systems. First, we demonstrated that LNP surface properties (e.g., fluidity) and intracellular delivery mechanisms (e.g., endocytosis versus fusion), are influenced by the RNA loading per LNP, even when the lipid composition remains unchanged. This highlights a crucial point: LNPs exhibit distinct properties depending on the cargo load, which may affect cellular uptake, biodistribution, and therapeutic efficacy. Prior studies have reported uneven RNA distribution in LNPs postformulation, especially with larger cargos like mRNA, where a significant portion of empty LNPs can be present.[50] Our results emphasize the importance of identifying and separating these empty LNPs, as their surface properties and intracellular dynamics differ significantly from those of RNA-loaded LNPs. For the same reason, our results suggest that empty LNPs should not be used as negative controls in LNP imaging or functional studies.

Second, our results highlight the need to reassess the factors influencing RNA efficacy in LNP systems. We demonstrated that lipid-siRNA organization affects several aspects of LNP intracellular behavior, including cellular uptake, RNA entry pathways, LNP dissociation within endosomes, and RNA escape from endosomes. These factors collectively impact RNA efficacy and should be considered when designing new LNPs. Currently, high-throughput screening efforts often focus on discovering novel ionizable lipids to improve RNA efficacy,[51] with an emphasis on their role in promoting endosomal escape. However, our data suggest that improved efficacy may also result from optimized lipid-RNA structural organization, not solely from the inherent properties of the ionizable lipids themselves. Incorporating lipid-RNA organization as a criterion in high-throughput studies could provide deeper insights into the mechanisms driving LNP efficacy. Beyond lipid composition, variations in RNA type and chemical modifications could also influence lipid-RNA organizations. For instance, mRNA-loaded LNPs can exhibit unique lipid-RNA organization in the form of "bleb-like" structures, with mRNA enrichment in the blebs potentially enhancing stability and efficacy.[9,12] Lipid-RNA organization may thus serve as a fundamental "fingerprint" property that governs LNP characteristics and intracellular dynamics. Understanding these dynamics is crucial, as they also provide stage-by-stage insights into the sequential events of intracellular delivery that affect RNA efficacy and how LNP architecture can be optimized to improve performance. For example, our single-particle imaging and light-activated siRNA release results indicate that the release of siRNA from LNPs into the endosomal compartment, rather than the downstream step from the endosomes to the cytosol, might represent a significant barrier to achieving efficient RNA delivery.

https://doi.org/10.1021/jacs.4c18308
J. Am. Chem. Soc. 2025, 147, 10430−10445

Third, our findings hold significant implications for stimuli-responsive or triggered-release LNP systems. In this study, we used light as a model stimulus to investigate how lipid-siRNA organization affects LNP responsiveness to external triggers. Our results showed that the degree of triggered release is closely tied to initial lipid-siRNA structural organization, which can be exploited to improve LNP performance. For instance, while LNPs with a low N/P ratio (NP1) face challenges such as ionizable lipids fully complexed with siRNA which is less efficient in promoting endosomal membrane disruption, they also exhibited more uniform helper lipid distribution throughout the LNP, leading to superior endosomal escape upon light activation compared to NP12. This demonstrated how suboptimal formulations can be improved with appropriate stimuli-responsive components based on its lipid-siRNA organization. These principles are not exclusive to light-based systems; other stimuli-responsive lipids, such as those sensitive to enzyme, pH or redox potential, may similarly rely on lipid-RNA structural organization for optimal functionality. The lipid-RNA organization determines when, where, and how these stimuli-responsive lipids interact with environmental triggers, ultimately affecting RNA efficacy. For example, when we incorporate pH-sensitive lipids into LNP to enhance their intracellular dissociation, a spatial organization where they are shielded in the LNP lumen could potentially prevent premature activation in acidic tumor microenvironments, reducing extracellular RNA leakage.

There are limitations to the current study warranting further inquiry in future studies. Most of our findings were obtained in cancer cell models, and lipid-siRNA organization might have different impacts for other cell types. Additionally, our investigations of lipid-siRNA organization were restricted to *in vitro* cellular models. *In vivo* studies are necessary to understand how lipid-RNA organization influences protein corona formation (binding type, rate, dissociation, etc.) and how protein binding may alter lipid distribution within LNPs.[52] These factors will be critical for future studies aimed at establishing clearer structure−function relationships in LNP design.

To conclude, lipid-siRNA organization plays a pivotal role in governing the intracellular dynamics and efficacy of siRNA-loaded LNPs. These findings offer new insights to help inform the rational design of LNP-based RNA delivery systems. We are excited for future work to explore the applicability of these principles to other types of nucleic acid cargos and stimuli-responsive LNP formulations.

MATERIALS AND METHODS

Materials. 1,2-Distearoyl-*sn*-glycero-3-phosphocholine (DSPC), cholesterol, 1,2-dimyristoyl-rac-glycero3-methoxy(poly(ethylene glycol))-2000 (DMG-PEG_{2000}), diethylene-triamine-penta-acetic acid-bis(stearylamide) (gadolinium salt) (DTPA-BSA(Gd)) were purchased from Avanti Polar Lipids (Alabaster, AL, USA). DLin-MC3-DMA was purchased from Nanosoft Polymers (NC, USA). Porphyrin-lipid was synthesized by the previously reported methods.[24]

Small Interfering RNA. All siRNAs were custom synthesized and purchased from Horizon Discovery (USA). siLuc: sense, 5′-GAU UAU GUC CGG UUA UGU AdTsdT-3′; antisense, 5′-UAC AUA ACC GGA CAU AAU CdTsdT-3′. For dye-labeled siRNA (FAM, Cy3, and Alexa-488 conjugated), the fluorophore was attached to the 5′ end of the sense strand.

Synthesis of LNPs. LNPs were synthesized using a microfluidic rapid mixing method as previously described.[28] Unless otherwise specified, lipids were mixed in ethanol at a molar ratio of 50:10:38.5:1.5 (DLin-MC3-DMA/Porphyrin-lipid/Cholesterol/DMG-PEG_{2000}). The siRNA was dissolved in 25 mM sodium acetate buffer (pH 4.0). The two phases were combined using herringbone microfluidic chips (Microfluidic ChipShop, Germany) at a volumetric flow rate ratio of 3:1 (aqueous to ethanol) with a total flow rate of 10 mL/min. The resulting solution was dialyzed against PBS (pH 7.4) overnight. Subsequently, the LNPs were concentrated using ultra centrifuge filters (Amicon, Sigma-Aldrich) and passed through 0.22 um filter before use.

For MC3-LNP, the lipid composition was adjusted to a molar ratio of 50:10:38.5:1.5 (DLin-MC3-DMA/DSPC/Cholesterol/DMG-PEG_{2000}). In the case of DTPA-BSA(Gd) incorporated MC3-LNP, the lipid composition followed a molar ratio of 50:10:2:36.5:1.5 (DLin-MC3-DMA/DSPC/DTPA-BSA(Gd)/Cholesterol/DMG-PEG_{2000})

For the singlet oxygen generation and porphyrin fluorescence quenching studies, the lipid composition followed a ratio of 50/1/9/38.5/1.5 mol % (MC3-lipid/Porphyrin-lipid/DSPC/Cholesterol/DMG-PEG_{2000}).

For the FRET study, the lipid composition was prepared at a molar ratio of 50/1/9/38.5/1.5 mol % (MC3-lipid/Porphyrin-lipid/DSPC/Cholesterol/DMG-PEG_{2000}). A fixed amount of Cy3-labeled siRNA was loaded across N/P ratios from 1 to 12, with the siRNA quantity standardized to the N/P = 12 condition. Unlabeled siRNA was added as needed at lower N/P ratios to achieve the desired N/P ratio.

For the confocal imaging of porphyrin-LNP cellular uptake, 10% (mol %) porphyrin-lipids were included in LNP formulation, and FAM-siRNA were loaded into the LNPs at N/P ratios ranging from 1 to 12.

For the light-induced siRNA endosomal escape study, LNPs incorporating 10% (mol/%) porphyrin-lipid were loaded with a fixed amount of FAM-labeled siRNA across N/P ratios from 1 to 12 (standardized to N/P = 12), with unlabeled siRNA added as needed to achieve the desired N/P ratio.

For the CLiC imaging studies, LNPs incorporating 10% porphyrin-lipid were loaded with an equal amount of Alexa488-siRNA across N/P ratios from 1 to 12 (standardized to N/P = 12). Unlabeled siRNA was added at lower N/P ratio condition to achieve the desired N/P ratio.

***In Vitro* Characterization of LNPs.** The hydrodynamic size, poly dispersity and zeta-potential of LNPs was characterized with a Zetasizer Nano ZS (Malvern Instruments). The morphology of Porphyrin-LNP was checked by Cyro-EM. Absorbance and fluorescence spectrum of Porphyrin-LNP was collected on a UV−vis spectrophotometer Cary 50 (Agilent) and Fluoromax fluorometer (Horiba Jobin Yvon) respectively. The porphyrin fluorescence quenching efficiency was calculated as follows:

$$Quenching\% = \left(1 - \frac{F_{intact}}{F_{disrupted}}\right) \times 100\%$$

F_{intact} and $F_{disrupted}$ refer to the fluorescence of porphyrin measured when porphyrin-LNPs are either intact in PBS or disrupted by 1% Triton X-100, respectively, at a porphyrin concentration of 1 μM.

siRNA concentration and encapsulation efficiency were measured by Quant-it RiboGreen RNA Assay based on manufacturer's protocol (Thermofisher). Briefly, LNPs were diluted in equal volumes of Tris-EDTA (TE) buffer or 2% Triton X-100 in TE buffer. Next, Ribogreen reagent was added into each sample well and incubated at 37 °C for 15 min before measuring its fluorescence intensities (Ex/Em: 480/520 nm). Fluorescence signal from TE buffer treated samples (F_{TE}) represents unencapsulated siRNA while fluorescence signal from TX-100 treated samples (F_{TX}) represents total siRNA. siRNA encapsulation efficiency can be determined as

$$Encapsulation\% = \frac{F_{TX} - F_{TE}}{F_{TX}} \times 100\%$$

Lipid Quantification by UPLC. The concentration of each lipid component in the LNP after synthesis was quantified using a ACQUITY UPLC H-Class system (Waters, Canada) with a BEH C18 column (1.7 μm, 2.1 × 50 mm). The mobile phases were (A) 80% (v/v) methanol in LC-grade water with 4 mM ammonium acetate, pH adjusted to 4.0 ± 0.1 with acetic acid, and (B) LC-grade methanol with 4 mM ammonium acetate. The flow rate was 0.6 mL/min, and the

https://doi.org/10.1021/jacs.4c18308
J. Am. Chem. Soc. 2025, 147, 10430−10445

column temperature was maintained at 50 °C. The sample injection volume was 5 μL. Gradient elution started at 95% phase A and 5% phase B, transitioning to 0% A and 100% B over 3.5 min, held for 2 min, then reverted to the initial condition.

Lipids standards were prepared across 15−350 μg/mL to generate standard curves based on the peak area and determine retention times: DMG-PEG_{2000} at 4.59 min, cholesterol at 4.66 min, porphyrin-lipid at 5.01 min, DSPC at 5.27 min, and MC3-lipid at 5.75 min. Lipid concentrations of each component in LNPs were quantified using the corresponding standard curves.

Cryo-EM Sample Preparation and Image Acquisition. LNPs were concentrated to approximately 10−15 mg/mL of total lipid and used immediately for preparing cryo-grids. Four μL of sample was deposited onto homemade holey gold grids glow-discharged at 15 mA for 30 s prior to plunge-freezing into liquid ethane using an FEI Mark IV Vitrobot. Blotting conditions of 2 s blotting, + 3 blot force, 5 °C ambient temperature, and 90% relative humidity were used. Cryo grids were loaded on a Glacios 200 kV microscope (ThermoFisher) and data sets were collected with EPU (ThermoFisher) at a nominal magnification of 92,000× magnification (1.566 Å per pixel) at a target defocus range of 1−3 μm.

Cryo-EM Image Processing. Image processing was performed in cryoSPARC (Structura Biotechnology) unless otherwise stated. Movies were aligned by patch motion correction and CTF parameters calculated by patch CTF estimation. An initial set of micrographs were used to train a custom crYOLO model[29] and used to autopick across all data sets. Picked coordinates on each micrograph were then manually curated to add or remove particles. Curated particle picks were then imported into cryoSPARC and used to extract particles with initial downsampling (800 pixels downsampld to 200 pixels). An initial round of 2D classification using a circular mask of 800−1000 Å was performed to drop bad particles and all particles kept were re-extracted with recentering and without downsampling. Re-extracted particles were then used for a final round of 2D classification.

Singlet Oxygen Measurement. Singlet oxygen ($^1O_2$) generation of Porphyrin-LNP was measured using singlet oxygen sensor green (SOSG, Invitrogen) assay. Briefly, SOSG solution was freshly prepared in methanol (5 mM) and diluted with PBS before mixing with Porphyrin-LNP samples (1 μM porphyrin), to have a final SOSG concentration of 10 μM. Samples were irradiated with a LED lightbox (Biolambda, Brazil) at 660 nm with a 50 mW/cm^2 irradiance to achieve light dose of 10 J/cm^2. Afterward, SOSG fluorescence was measured by a CLARIOstar platereader (BMG LABTECH) at 488 nm excitation and 525 nm emission.

FRET Experiment. For the FRET experiment, Cy3-siRNA was loaded into porphyrin-LNPs, formulated with 1% porphyrin-lipid and 9% DSPC. To minimize fluorescence changes due to Cy3 concentration, an equal amount of Cy3-siRNA was loaded into the LNPs at N/P ratios ranging from 1 to 12. For lower N/P ratios, Cy3-siRNA was mixed with nonlabeled siRNA to achieve the desired siRNA amount. LNP samples were diluted in PBS or 2% TX-100 to a final Cy3-siRNA concentration of 200 nM prior to fluorescence measurements using a CLARIOstar plate reader (Ex/Em: 522/550−800 nm).

LNP Membrane Fluidity Measurement. The LNPs were diluted in PBS to a final total lipid concentration of 100 μM. C-laurdan (TOCRIS) was added to the LNP suspension at a concentration of 10 μM. Fluorescence was measured for LNP samples, both in the presence and absence of C-laurdan, using a Fluoromax fluorometer (Ex/Em: 350/400−550 nm). The emission spectra of C-laurdan in the presence of LNPs were determined by subtracting the fluorescence of LNPs alone from that of the C-laurdan-containing samples. Generalized polarization (GP) values were subsequently computed using the following formula:

$$GP = \frac{I_{420-460} - I_{470-510}}{I_{420-460} + I_{470-510}}$$

Here, $I_{420-460}$ and $I_{470-510}$ is the sum of the fluorescence intensities between 420 and 460 nm and 470−510 nm. GP value can vary between −1 to 1, with lower GP value representing higher membrane fluidity and higher GP value suggesting higher rigidity.

Cu^{2+} Chelation on Porphyrin-LNP. Copper acetate was dissolved in molecular biology grade water (DNase/RNase-free) to a final concentration of 100 mM Cu^{2+}. Lipid nanoparticle (LNP)−siRNA samples with varying N/P ratios were prepared at a porphyrin-lipid concentration of 0.2 mM. For chelation, 50 μL of LNP−siRNA was mixed with 350 μL of the copper solution and incubated at 35 °C, 300 rpm, maintaining a 3500:1 copper/porphyrin-lipid molar ratio. Samples were collected at various time points for UPLC-MS analysis to assess chelation efficiency. To optimize chelation conditions, LNPs were diluted 4-fold in methanol to disrupt nanoparticles, followed by copper addition. Chelation was completed within 5 min, as shown in Figure S9.

Chelation rates were measured using a UPLC−ESI-MS system (Waters Acquity UPLC, triple quadrupole MS, CSH Phenyl-Hexyl column, Waters, Canada). The UPLC method involved a gradient from 60% solvent A (0.1% TFA)/40% solvent B (acetonitrile) to 0% A/100% B over 3 min, held for 1 min, and then returned to the initial conditions. The column temperature was set to 60 °C with a flow rate of 0.6 mL/min.

Unlabeled porphyrin-lipid eluted at 2.9 min (Q-band at 666 nm, calculated mass: 1012.26, observed $[M]^+$: 1013.67), while porphyrin-(Cu)-lipid eluted at 3.1 min (Q-band at 653 nm, calculated mass: 1073.79, observed $[M]^+$: 1074.49). Chelation efficiency was calculated as the ratio of porphyrin(Cu)-lipid peak intensity to the total intensity of unlabeled and chelated porphyrin-lipid.

Cell Culture and LNP Cellular Uptake Imaging. PC-3M-luc-C6 (PC3-Luc6) and KB cells were cultured in Eagle's Minimum Essential Medium (supplemented with 10% FBS). All the cell lines were maintained at 37 °C under 5% CO_2. For cellular uptake imaging studies, cells were seeded into 8-well coverglass-bottom chambers (Nunc LabTek, Sigma−Aldrich, Rochester, NY) at a cell-seeding density of 2 × 10^4 cells per well. After 48 h, Porphyrin-LNPs load with FAM-siRNA were added at a concentration of 2 μM (based on porphyrin) and incubated for 6 h. Cells were then washed twice with culturing medium before imaging. Fluorescence images were captured by Leica TCS SP8 STED confocal microscope equipped with a 63x oil objective lens. Customized filter settings were used to collect signal from porphyrin-lipid (excitation: 633 nm; emission: 670−765 nm, laser power 3%), and FAM-labeled siRNA (excitation: 488 nm; emission: 507−580 nm, laser power 60%).

For cellular uptake pathway studies, inhibitors were added 30 min before adding LNPs at concentrations of bafilomycin A1 (1 μM), 5-(*N*-ethyl-*N*-isopropyl)-Amiloride (EIPA) (50 μM) and chlorpromazine (CPZ) (10 μg/mL). All other procedures followed the standard imaging protocol. For the low temperature study, cells were preincubated at 4 °C for 30 min, then incubated with LNPs at 4 °C for 3 h before imaging. For ATP depletion, cells were pretreated at 37 °C with sodium azide (20 mM) and 2-deoxy-D-glucose (50 mM) for 30 min, followed by a 2-h LNP incubation under the same conditions.

Quantitative Cellular Uptake of LNPs. Briefly, PC3-Luc6 cells were seeded into 24-well plates at a seeding density of 2.5 × 10^4 cells per well and waited 48 h before adding LNPs at a concentration of 2 μM (based on porphyrin) or the equivalent 12 μM (based on total lipid) and incubated for given time points. Afterward, the cells were trpsinized and the number of cells in each well were counted by a cell counter (DeNovix, US). Next, for quantification of porphyrin LNP uptake, the cells were further fully digested with DMSO to disrupt all the LNP and make sure porphyrin fluorescence was not quenched. Then its fluorescence was measured with CLARIOstar plate reader (Ex/Em: 410/600−800 nm); For quantification of MC3-LNP uptake, since there is no fluorescent label, 2% DTPA-BSA(Gd) lipid was included in the LNP formulation, so that Gd^{3+} can be quantified by inductively coupled plasma mass spectrometry (ICP-MS) as a measurement of total lipid uptake. After cell counting, the cell suspension was transferred to 2 mL capped Eppendorf tube before drying out by SpeedVac (ThermoFisher). Subsequently, all samples were digested in a 3:1 mixture of 70% w/v nitric acid and concentrated 37% w/v hydrochloric acid for 24 h. Samples were diluted with ultrapure water (ddH_2O). for quantitative Gd^{3+} ion measurement using a NexION 350

https://doi.org/10.1021/jacs.4c18308
J. Am. Chem. Soc. 2025, 147, 10430−10445

× ICP-MS (PerkinElmer). A calibration curve ranging from 1×10^{-6} to 1×10^{-2} mg·L^{-1} of elemental Gd^{3+} (High-Purity Standards) prepared in 2% (v/v) HNO_3 was generated to determine the quantity of Gd^{3+} in each sample and finally normalized against cell count.

***In Vitro* Luciferase Knockdown.** PC3-Luc6 cells were seeded at 4000 cells per well into 96-well plates for 48 h. Then cells were incubated with LNPs at different siRNA concentration overnight, after which the cells were washed twice with culturing medium and the wells were replaced with medium that contains 0.05 mg/mL alamarBlue (Invitrogen) for viability measurement: cells were incubated for 2 h, after which fluorescence emission was collected using a CLARIOstar microplate reader (excitation of 540/8 nm and emission of 590/8 nm). Luciferase expression of PC3-Luc6 on the same plate was evaluated through bioluminescence: after alamarBlue assay, 5 μL D-luciferin solution (25 mM) was added into each well (100 μL medium), after which the bioluminescence was collected by IVIS Spectrum *In vivo* Imaging System (PerkinElmer). Bioluminescence intensity of each well was further normalized by its viability before analysis.

Confocal Imaging of Light-Induced siRNA Endosomal Escape. Cells were seeded into 8-well coverglass-bottom chambers (Nunc LabTek, Sigma−Aldrich, Rochester, NY) at a cell-seeding density of 2×10^4 cells per well. After 48 h, Porphyrin-LNPs load with FAM-siRNA were added at a concentration of 2 μM (based on porphyrin) and incubated for 6 h before imaging. Cells were then washed twice with culturing medium before imaging. Fluorescence images were captured by Leica STED microscopy using a 63× oil objective lens. Customized filter settings were used to collect signal: 488 nm laser was used to excite both FAM and porphyrin at a power of 80% with two different HyD detectors at 507−580 nm (FAM) and 640 nm-765 nm (porphyrin) collecting their fluorescence, respectively. During light irradiation, porphyrin-lipid was irradiated at 660 nm and the laser power was raised to 100% for given time intervals. Laser power and detector gain adjustment were kept consistent before and post laser irradiation.

To quantify FAM intracellular fluorescent intensity, raw images were processed in Fiji (ImageJ), applying a threshold to isolate fluorescence from punctate organelles (example provided in Figure S20). A region of interest (ROI) was then created for a single cell. The total fluorescence intensity sum and area for the whole cell and organelles was quantified separately, along with the organelle area. The cytosolic fluorescence was determined by subtracting organelle fluorescence from the total cell fluorescence.

Single-Particle CLiC Imaging. The CLiC imaging device consists of a flow cell constructed with a top glass coverslip (25 mm × 25 mm, 150 ± 20 μm thick) and a bottom glass coverslip (25 mm × 25 mm, 200 ± 10 μm thick) containing an array of microwells.[19] The microwells were fabricated through dry etching via reactive ion etching (RIE) technique.[53] As previously described,[19,54] the top and bottom coverslips were passivated with polyethylene glycol (PEG) layers utilizing silane chemistry and a cloud point PEGylation process. The flow cell was mounted in a custom CLiC microfluidic chuck for imaging.

The Leslie lab microscope setup and imaging procedures followed previously reported protocols.[49] Briefly, a ScopeSys nanopositioner was used to precisely lower the CLiC lens, which deflected the top layer of the flow cell downward, confining particles within the microwell array. For imaging, 50 μL of LNP samples at varying N/P ratios, with concentrations ranging from 1.32 μM to 1.59 μM, were added to the flow cell via the inlet of the chuck. The LNP concentrations were adjusted to achieve single-particle confinement per microwell across different formulations. The CLiC device was mounted on a Nikon Ti-E inverted microscope equipped with two Andor iXon Ultra 897 EMCCD cameras (pixel size: 16 μm/pixel) and a 100× oil immersion objective lens (Apochromat TIRF, N.A. 1.49, W.D. 0.12 mm, F.O.V 22 mm). The porphyrin-LNP samples were excited using a 647 nm Coherent Obis laser and a 488 nm Coherent Sapphire LP laser. Customized optimal emission filter settings were used for Alexa 488 (525 ± 50 nm, part number: Chroma ET525/50m) and porphyrin-lipid (680 ± 40 nm, part number: Chroma ET680/40m) to reduce bleed-through of fluorescence. Using a long-pass dichroic filter (Chroma ET640lp), the fluorescence signals from the Alexa 488 and Porphyrin dyes were separated, and the two channels were imaged on different Andor cameras. The exposure time and laser powers were 20 ms and 3.4 mW (488 nm laser) and 4.2 mW (647 nm laser), respectively. For single-particle imaging video acquisition, both lasers were turned on for 1 s to record preburst conditions, followed by 40 s of 647 nm laser exposure to burst the LNPs. Both lasers were then activated for an additional 2 s to capture postburst conditions.

CLiC Single-Particle Image Processing. The fluorescence intensities of individual, freely diffusing particles in the LNP channel in Figure 6c were determined as previously described.[19] Fluorescent intensities from individual particles were detected and tracked by fitting a 2D symmetric Gaussian to each frame. The resulting Gaussian fits to individual particles were then integrated to obtained total fluorescent signals per particle.

For "fast-diffusing" siRNA molecules (e.g., Alexa 488-labeled siRNA in Figure 6c), the fluorescence was quantified by averaging the intensities of individual microwells. This was accomplished by first identifying microwells and then calculating the average fluorescence intensity per microwell per frame, as previously reported.[49]

■ ASSOCIATED CONTENT

Supporting Information

The Supporting Information is available free of charge at https://pubs.acs.org/doi/10.1021/jacs.4c18308.

Additional experimental details, methods, LNP characterizations, and intracellular imaging results (PDF)

CLiC imaging of LNP (NP1) burst event upon light (Video S1)(AVI)

CLiC imaging of LNP (NP3) burst event upon light (Video S2) (AVI)

CLiC imaging of LNP (NP6) burst event upon light (Video S3) (AVI)

CLiC imaging of LNP (NP12) burst event upon light (Video S4) (AVI)

■ AUTHOR INFORMATION

Corresponding Authors

Juan Chen − *Princess Margaret Cancer Center, University Health Network, Toronto, Ontario M5G 1L7, Canada*; Email: juan.chen@uhn.ca

Gang Zheng − *Institute of Medical Science, University of Toronto, Toronto, Ontario M5G 1L7, Canada; Princess Margaret Cancer Center, University Health Network, Toronto, Ontario M5G 1L7, Canada; Department of Medical Biophysics, University of Toronto, Toronto, Ontario M5G 1L7, Canada*; orcid.org/0000-0002-0705-7398; Email: gang.zheng@uhn.ca

Authors

Yulin Mo − *Institute of Medical Science, University of Toronto, Toronto, Ontario M5G 1L7, Canada; Princess Margaret Cancer Center, University Health Network, Toronto, Ontario M5G 1L7, Canada*; orcid.org/0009-0006-7716-905X

Alexander F. A. Keszei − *Princess Margaret Cancer Center, University Health Network, Toronto, Ontario M5G 1L7, Canada*

Shagun Kothari − *Michael Smith Laboratories and Department of Physics, University of British Columbia, Vancouver, British Columbia V6T 1Z4, Canada*

Heyi Liu − *Princess Margaret Cancer Center, University Health Network, Toronto, Ontario M5G 1L7, Canada*

Anni Pan − *Princess Margaret Cancer Center, University Health Network, Toronto, Ontario M5G 1L7, Canada*

Paige Kim − *Princess Margaret Cancer Center, University Health Network, Toronto, Ontario M5G 1L7, Canada*
Jiachuan Bu − *Princess Margaret Cancer Center, University Health Network, Toronto, Ontario M5G 1L7, Canada*
Albert Kamanzi − *Michael Smith Laboratories and Department of Physics, University of British Columbia, Vancouver, British Columbia V6T 1Z4, Canada;* orcid.org/0000-0002-6790-1140
David L. Dai − *Princess Margaret Cancer Center, University Health Network, Toronto, Ontario M5G 1L7, Canada; Department of Medical Biophysics, University of Toronto, Toronto, Ontario M5G 1L7, Canada*
Mohammad T. Mazhab-Jafari − *Princess Margaret Cancer Center, University Health Network, Toronto, Ontario M5G 1L7, Canada; Department of Medical Biophysics, University of Toronto, Toronto, Ontario M5G 1L7, Canada*
Sabrina Leslie − *Michael Smith Laboratories and Department of Physics, University of British Columbia, Vancouver, British Columbia V6T 1Z4, Canada*

Complete contact information is available at: https://pubs.acs.org/10.1021/jacs.4c18308

Notes

The authors declare no competing financial interest.

■ ACKNOWLEDGMENTS

The authors would like to acknowledge the Princess Margaret RNA Medicine Core and Advanced Optical Microscopy Facility (University Health Network, Toronto) for technical support. The Quantum Matter Institute at UBC supported the microfabrication of the wells, with assistance from technician Michelle Peliova in the Leslie Lab. This work was funded by the support of the Princess Margaret Discovery to Impact Grant, Terry Fox New Frontiers Program Project Grant (#1137), NanoMedicines Innovation Network (NMIN), the Canadian Institutes of Health Research, and the Canada Research Chairs Program (950-232468). Y.M. is funded by the Centre for Pharmaceutical Oncology (CPO) Scholarship, Peterborough K.M. HUNTER Charitable Foundation Graduate Award and NMIN doctoral award. A.K. is funded by a MITACS Elevate Fellowship sponsored by ScopeSys. S.K. is funded by an NMIN MSc Fellowship and Dr. Leslie's NSERC Discovery and UBC's Michael Smith Laboratories startup funding from the Department of Physics and Astronomy. Dr. Leslie's Killam Accelerator Research Fellowship (KARF) also contributed to this research. The Canadian Foundation for Innovation supported the microscopy infrastructure in the Leslie Laboratories. A.F.A.K, D.L.D., and M.M.-J. were supported by PMCF. ThermoFisher Scientific Glacios 200 kV transmission electron microscope was funded by Canada Foundation for Innovation (CFI) and Ontario Research Fund-Research Innovation (ORF-RI)

■ REFERENCES

(1) Cullis, P. R.; Felgner, P. L. The 60-year evolution of lipid nanoparticles for nucleic acid delivery. *Nat. Rev. Drug Discovery* **2024**, *23*, 709−722.
(2) Kulkarni, J. A. The current landscape of nucleic acid therapeutics. *Nat. Nanotechnol.* **2021**, *16*, 630−643.
(3) Kulkarni, J. A.; Witzigmann, D.; Chen, S.; Cullis, P. R.; van der Meel, R. Lipid Nanoparticle Technology for Clinical Translation of siRNA Therapeutics. *Acc. Chem. Res.* **2019**, *52*, 2435−2444.
(4) Akinc, A. The Onpattro story and the clinical translation of nanomedicines containing nucleic acid-based drugs. *Nat. Nanotechnol.* **2019**, *14*, 1084−1087.
(5) Polack, F. P. Safety and Efficacy of the BNT162b2 mRNA COVID-19 Vaccine. *N. Engl. J. Med.* **2020**, *383*, 2603−2615.
(6) *MAGNITUDE: A Phase 3 Study of NTLA-2001 in Participants With Transthyretin Amyloidosis With Cardiomyopathy (ATTR-CM).* https://clinicaltrials.gov/study/NCT06128629.
(7) Kulkarni, J. A. On the Formation and Morphology of Lipid Nanoparticles Containing Ionizable Cationic Lipids and siRNA. *ACS Nano* **2018**, *12*, 4787−4795.
(8) Kulkarni, J. A.; Witzigmann, D.; Leung, J.; C. Tam, Y. Y. C.; Cullis, P. R. On the role of helper lipids in lipid nanoparticle formulations of siRNA. *Nanoscale* **2019**, *11*, 21733−21739.
(9) Brader, M. L. Encapsulation state of messenger RNA inside lipid nanoparticles. *Biophys. J.* **2021**, *120*, 2766−2770.
(10) Zheng, L.; Bandara, S. R.; Tan, Z.; Leal, C. Lipid nanoparticle topology regulates endosomal escape and delivery of RNA to the cytoplasm. *Proc. Natl. Acad. Sci. U. S. A.* **2023**, *120*, No. e2301067120.
(11) Pattipeiluhu, R.; Zeng, Y.; Hendrix, M. M. R. M.; Voets, I. K.; Kros, A.; Sharp, T. H. Liquid crystalline inverted lipid phases encapsulating siRNA enhance lipid nanoparticle mediated transfection. *Nat. Commun.* **2024**, *15*, 1303.
(12) Cheng, M. H. Y.; Leung, J.; Zhang, Y.; Strong, C.; Basha, G.; Momeni, A.; Chen, Y.; Jan, E.; Abdolahzadeh, A.; Wang, X.; et al. Induction of Bleb Structures in Lipid Nanoparticle Formulations of mRNA Leads to Improved Transfection Potency. *Adv. Mater.* **2023**, *35*, 2303370.
(13) Patel, S.; Ashwanikumar, N.; Robinson, E.; Xia, Y.; Mihai, C.; Griffith, J. P.; Hou, S.; Esposito, A. A.; Ketova, T.; Welsher, K.; et al. Naturally-occurring cholesterol analogues in lipid nanoparticles induce polymorphic shape and enhance intracellular delivery of mRNA. *Nat. Commun.* **2020**, *11*, 983.
(14) Thelen, J. L. Morphological Characterization of Self-Amplifying mRNA Lipid Nanoparticles. *ACS Nano* **2024**, *18*, 1464−1476.
(15) Wittrup, A.; Lieberman, J. Knocking down disease: A progress report on siRNA therapeutics. *Nat. Rev. Genet.* **2015**, *16*, 543−552.
(16) Setten, R. L.; Rossi, J. J.; Han, S. The current state and future directions of RNAi-based therapeutics. *Nat. Rev. Drug Discovery* **2019**, *18*, 421−446.
(17) Bakrania, A.; Mo, Y.; Zheng, G.; Bhat, M. RNA nanomedicine in liver diseases. *Hepatology* **2024**, 10−1097.
(18) Hoy, S. M. Patisiran: First Global Approval. *Drugs* **2018**, *78*, 1625−1631.
(19) Kamanzi, A. Simultaneous, Single-Particle Measurements of Size and Loading Give Insights into the Structure of Drug-Delivery Nanoparticles. *ACS Nano* **2021**, *15*, 19244−19255.
(20) Wittrup, A. Visualizing lipid-formulated siRNA release from endosomes and target gene knockdown. *Nat. Biotechnol.* **2015**, *33*, 870−876.
(21) Gilleron, J. Image-based analysis of lipid nanoparticle−mediated siRNA delivery, intracellular trafficking and endosomal escape. *Nat. Biotechnol.* **2013**, *31*, 638−646.
(22) Du Rietz, H.; Hedlund, H.; Wilhelmson, S.; Nordenfelt, P.; Wittrup, A. Imaging small molecule-induced endosomal escape of siRNA. *Nat. Commun.* **2020**, *11*, 1809.
(23) Hedlund, H.; Du Rietz, H.; Johansson, J. M.; Eriksson, H. C.; Zedan, W.; Huang, L.; Wallin, J.; Wittrup, A. Single-cell quantification and dose-response of cytosolic siRNA delivery. *Nat. Commun.* **2023**, *14*, 1075.
(24) Lovell, J. F. Porphysome nanovesicles generated by porphyrin bilayers for use as multimodal biophotonic contrast agents. *Nat. Mater.* **2011**, *10*, 324−332.
(25) Huynh, E.; Zheng, G. Porphysome nanotechnology: A paradigm shift in lipid-based supramolecular structures. *Nano Today* **2014**, *9*, 212−222.
(26) Rajora, M. A.; Lou, J. W. H.; Zheng, G. Advancing porphyrin's biomedical utility via supramolecular chemistry. *Chem. Soc. Rev.* **2017**, *46*, 6433−6469.

(27) Mo, Y. Light-Activated siRNA Endosomal Release (LASER) by Porphyrin Lipid Nanoparticles. *ACS Nano* **2023**, *17*, 4688−4703.
(28) Belliveau, N. M. Microfluidic Synthesis of Highly Potent Limit-size Lipid Nanoparticles for In Vivo Delivery of siRNA. *Mol. Ther. -Nucleic Acids* **2012**, *1*, No. e37.
(29) Wagner, T.; Merino, F.; Stabrin, M.; Moriya, T.; Antoni, C.; Apelbaum, A.; Hagel, P.; Sitsel, O.; Raisch, T.; Prumbaum, D.; et al. SPHIRE-crYOLO is a fast and accurate fully automated particle picker for cryo-EM. *Commun. Biol* **2019**, *2*, 218.
(30) Kim, H. M. A Two-Photon Fluorescent Probe for Lipid Raft Imaging: C-Laurdan. *ChemBioChem* **2007**, *8*, 553−559.
(31) Takechi-Haraya, Y. Atomic Force Microscopic Analysis of the Effect of Lipid Composition on Liposome Membrane Rigidity. *Langmuir* **2016**, *32*, 6074−6082.
(32) Liu, T. W.; MacDonald, T. D.; Shi, J.; Wilson, B. C.; Zheng, G. Intrinsically Copper-64-Labeled Organic Nanoparticles as Radiotracers. *Angew. Chem., Int. Ed.* **2012**, *51*, 13128−13131.
(33) MacDonald, T. D.; Liu, T. W.; Zheng, G. An MRI-Sensitive, Non-Photobleachable Porphysome Photothermal Agent. *Angew. Chem., Int. Ed.* **2014**, *53*, 6956−6959.
(34) Shao, S. Functionalization of cobalt porphyrin−phospholipid bilayers with his-tagged ligands and antigens. *Nat. Chem.* **2015**, *7*, 438−446.
(35) Kerr, M. C.; Teasdale, R. D. Defining Macropinocytosis. *Traffic* **2009**, *10*, 364−371.
(36) Mercer, J.; Helenius, A. Virus entry by macropinocytosis. *Nat. Cell Biol.* **2009**, *11*, 510−520.
(37) Lin, Q. Imaging the Cytosolic Drug Delivery Mechanism of HDL-Like Nanoparticles. *Pharm. Res.* **2014**, *31*, 1438−1449.
(38) Maugeri, M.; Nawaz, M.; Papadimitriou, A.; Angerfors, A.; Camponeschi, A.; Na, M.; Hölttä, M.; Skantze, P.; Johansson, S.; Sundqvist, M.; et al. Linkage between endosomal escape of LNP-mRNA and loading into EVs for transport to other cells. *Nat. Commun.* **2019**, *10*, 4333.
(39) Sahay, G. Efficiency of siRNA delivery by lipid nanoparticles is limited by endocytic recycling. *Nat. Biotechnol.* **2013**, *31*, 653−658.
(40) Yoshimori, T.; Yamamoto, A.; Moriyama, Y.; Futai, M.; Tashiro, Y. Bafilomycin A1, a specific inhibitor of vacuolar-type H(+)-ATPase, inhibits acidification and protein degradation in lysosomes of cultured cells. *J. Biol. Chem.* **1991**, *266*, 17707−17712.
(41) Racoosin, E. L.; Swanson, J. A. Macropinosome maturation and fusion with tubular lysosomes in macrophages. *J. Cell Biol.* **1993**, *121*, 1011−1020.
(42) Koivusalo, M. Amiloride inhibits macropinocytosis by lowering submembranous pH and preventing Rac1 and Cdc42 signaling. *J. Cell Biol.* **2010**, *188*, 547−563.
(43) Ramirez, C.; Hauser, A. D.; Vucic, E. A.; Bar-Sagi, D. Plasma membrane V-ATPase controls oncogenic RAS-induced macropinocytosis. *Nature* **2019**, *576*, 477−481.
(44) Schwoebel, E. D.; Ho, T. H.; Moore, M. S. The mechanism of inhibition of Ran-dependent nuclear transport by cellular ATP depletion. *J. Cell Biol.* **2002**, *157*, 963−974.
(45) Chen, D.; Ganesh, S.; Wang, W.; Amiji, M. The role of surface chemistry in serum protein corona-mediated cellular delivery and gene silencing with lipid nanoparticles. *Nanoscale* **2019**, *11*, 8760−8775.
(46) Ren, J. Chemical and Biophysical Signatures of the Protein Corona in Nanomedicine. *J. Am. Chem. Soc.* **2022**, *144*, 9184−9205.
(47) Cullis, P. R.; Hope, M. J. Lipid Nanoparticle Systems for Enabling Gene Therapies. *Mol. Ther.* **2017**, *25*, 1467−1475.
(48) Luo, D. Rapid Light-Triggered Drug Release in Liposomes Containing Small Amounts of Unsaturated and Porphyrin−Phospholipids. *Small* **2016**, *12*, 3039−3047.
(49) Kamanzi, A. Quantitative Visualization of Lipid Nanoparticle Fusion as a Function of Formulation and Process Parameters. *ACS Nano* **2024**, *18*, 18191−18201.
(50) Li, S.; Hu, Y.; Li, A.; Lin, J.; Hsieh, K.; Schneiderman, Z.; Zhang, P.; Zhu, Y.; Qiu, C.; Kokkoli, E.; et al. Payload distribution and capacity of mRNA lipid nanoparticles. *Nat. Commun.* **2022**, *13*, 5561.
(51) Zhang, Y.; Sun, C.; Wang, C.; Jankovic, K. E.; Dong, Y. Lipids and Lipid Derivatives for RNA Delivery. *Chem. Rev.* **2021**, *121*, 12181−12277.
(52) Sebastiani, F. Apolipoprotein E Binding Drives Structural and Compositional Rearrangement of mRNA-Containing Lipid Nanoparticles. *ACS Nano* **2021**, *15*, 6709−6722.
(53) Henkin, G. Manipulating and Visualizing Molecular Interactions in Customized Nanoscale Spaces. *Anal. Chem.* **2016**, *88*, 11100−11107.
(54) Emilsson, G. Strongly Stretched Protein Resistant Poly(ethylene glycol) Brushes Prepared by Grafting-To. *ACS Appl. Mater. Interfaces* **2015**, *7*, 7505−7515.

https://doi.org/10.1021/jacs.4c18308
J. Am. Chem. Soc. 2025, 147, 10430−10445